




A Multiparametric Nonlinear Regression Approach for the Estimation of Global Surface Ocean pCO₂ Using Satellite Oceanographic Data

Kande Vamsi Krishna , Palanisamy Shanmugam , and Pullaiahgari Venkata Nagamani 

Abstract—Estimation of the partial pressure of carbon dioxide (pCO₂) and its space–time variability in global surface ocean waters is essential for understanding the carbon cycle and predicting the future atmospheric CO₂ concentration. Until recently, only basin-scale distribution of pCO₂ has been reported by using satellite-derived climatological data due to the lack of models for global-scale applications. In the present work, a multiparametric nonlinear regression (MPNR) for the estimation of global-scale distribution of pCO₂ on the ocean surface is developed using continuous *in-situ* measurements of pCO₂, chlorophyll-*a* (Chl_a) concentration, sea surface temperature (SST), and sea surface salinity (SSS) obtained on a number of cruise programs in various regional oceanic waters. Analysis of these measurement data showed strong relationships of pCO₂ with Chl_a, SST, and SSS, because these three parameters are governed by the complex interactions of oceanographic processes (physical, biological, and chemical) and meteorological processes and thus influence pCO₂ levels over different spatial and temporal scales. In order to account for regional differences in the influences of these processes on pCO₂, model parameterizations are derived as a function of Chl_a, SST, and SSS data with different boundary conditions. Because the strength of each influencing parameters on pCO₂ differed at different Chl_a, SST, and SSS ranges, measurement data were grouped with reference to the Chl_a, SST, and SSS ranges and significant correlations of the pCO₂ with dominant processes were established: for example, an inverse correlation of the pCO₂ with Chl_a, SST, and SSS in polar and subpolar regions, a positive correlation of the pCO₂ with SST and SSS and an inverse correlation of the pCO₂ with Chl_a in tropical and subtropical regions, and an inverse correlation of the pCO₂ with SST and a positive correlation of the pCO₂ with Chl_a and SSS in equatorial regions. This indicates that the relationship of pCO₂ versus biological and physical parameters is more complex and an individual parameter alone would not serve as an accurate estimator of basin- and global-scale pCO₂ trends. Thus, changes in Chl_a, SST, and SSS were systematically analyzed as they account for biological and physical effects on pCO₂ and best constrained based upon their strong relationships with pCO₂ using the MPNR regression approach. The accuracy of the MPNR was assessed using independent *in-situ* data and satellite pCO₂ data

derived from global Level-3 Chl_a, SST, and SSS data. Validation results showed that satellite-derived pCO₂ data agreed with direct *in-situ* pCO₂ measurements with an RMSE 6.68–7.5 μatm and a relative error less than 5%, which is significantly small as compared to the errors associated with earlier satellite pCO₂ computations. The distribution and magnitude of spatial and temporal (monthly and seasonal) amplitude of satellite-derived pCO₂ in climatic zones and ocean basins were further examined and agreed well with the shipboard pCO₂ observations and climatological surface ocean pCO₂ data.

Index Terms—Carbon dioxide, chlorophyll-*a*, multiparametric algorithm, partial pressure of carbon dioxide, satellite oceanography, sea surface salinity, sea surface temperature.

I. INTRODUCTION

PARTIAL pressure of carbon dioxide (pCO₂ expressed by a unit of μatm) in surface ocean waters is a key parameter used to study ocean CO₂ absorption, acidification, primary productivity, carbon cycle, source, and sinks of CO₂, and biogeochemistry. Due to the increasing levels of atmospheric CO₂ caused by anthropogenic emissions (e.g., burning of fossil fuels, deforestation, population growth, land use changes, and industrial processes) [1]–[3], there is noticeable gradient difference between atmospheric and oceanic CO₂ concentrations that is likely to be further affected by climate-driven changes and warming scenarios [4], [5]. It has been shown that the surface ocean exhibits a much larger spatial and temporal variability in the CO₂ flux compared to the atmosphere owing to the variable contribution processes other than the ocean carbon sink, such as upwelling, eddies, and physical mixing [6]–[8]. Presently, ocean–atmosphere exchange is estimated to be approximately 1.5–2 Gt of carbon per annum [8]. The change of sign in CO₂ flux between sources and sinks largely depends on major controlling mechanisms, such as physical pump, biological pump, and solubility pump [9]–[11]. Major sources of CO₂ are respiration and decay of biological organisms and major sinks are photosynthesis by phytoplankton and construction of carbonate shells, which contribute significantly to the observed pCO₂ variability in the global ocean [12]. To date, much less is known about the spatial structures and temporal variability of basin- and global-scales of the CO₂ exchange because of the limited observations. Thus, it is essential to improve our knowledge on the global-scale spatial and temporal variability in the pCO₂ distribution for better understanding the response of the ocean carbon sink to increasing atmospheric CO₂ and the

Manuscript received February 11, 2020; revised August 19, 2020 and September 12, 2020; accepted September 18, 2020. Date of publication September 24, 2020; date of current version October 22, 2020. This work was supported by the IIT Madras through the MHRD fellowship and the ISRO-IITM Cell under Grant OEC1718175ISROPSHA. (Corresponding author: Palanisamy Shanmugam.)

Kande Vamsi Krishna and Palanisamy Shanmugam are with the Ocean Optics and Imaging Laboratory, Department of Ocean Engineering, IIT Madras, Chennai 600036, India (e-mail: kvamsikrishnaiit@gmail.com; pshanmugam@iitm.ac.in).

Pullaiahgari Venkata Nagamani is with Ocean Satellite Group, National Remote Sensing Center (NRSC), ISRO, Hyderabad 500037, India (e-mail: pvnagamani@gmail.com).

Digital Object Identifier 10.1109/JSTARS.2020.3026363

climate-driven feedbacks and predicting its future trends. This requires to accurately estimate basin- and global-scale pCO₂ trends using decades of satellite data.

Surface ocean pCO₂ variations are mainly influenced by thermodynamic, biological (production and respiration), and physical mixing processes [13] due to sea surface temperature (SST), sea surface salinity (SSS), chlorophyll-a (Chla), mixed layer depth (MLD), colored dissolved organic matter (CDOM), net primary productivity (NPP), photosynthetically active radiation (PAR), wind speed, and other factors. With the advent of remote sensing technology and data processing/retrieval algorithms, many of these parameters can be easily and accurately derived from satellite data that provide advantages over the expensive *in-situ* measurements in terms of spatial and temporal analysis in large scales. In the past decades, a number of remote sensing methods have been developed for the estimation of pCO₂ using satellite oceanographic data; for example, multiple linear regression (MLR) [14]–[18], multiple nonlinear regression (MNR) [19], [20], multiple polynomial regression (MPR) [21], [22], random forest regression (RFR) [23], principle component analysis (PCA) [24], [25], self-organizing map (SOM) [20], [26], [27] Kohonen feature map (KFM) [28], feed forward neural network (FFNN) [29], [30], feed forward back propagation (FFBP) [31], machine learning analysis (MLA) [32], mechanistic semianalytical algorithm (MeSAA) [13], [33], and quasimechanistic approaches [34]. These methods provide fairly accurate estimations of regional-scale or basin-scale pCO₂ and yield significant uncertainties in the global-scale pCO₂ distribution due to the limited *in-situ* data or oversimplified/generalized model parameterizations. Significant uncertainties in the pCO₂ distribution can also be attributed to the inaccurate satellite oceanographic data products.

On a regional or basin-scale, MLR estimated pCO₂ as a function of SST and longitude in North Pacific Ocean waters [18]. It was observed that the subtropical North Pacific Ocean pCO₂ levels are chiefly controlled by the SST, and consequently, the satellite-derived pCO₂ agreed well with the *in-situ* measurements with an RMSE deviation of $\pm 17 \mu\text{atm}$. However, this approach yielded a higher RMSE deviation ($\pm 40 \mu\text{atm}$) in Northwestern subpolar regions caused by the influence of other effects, such as seasonal changes in biological production, mixing with subsurface waters, and air–sea exchange of CO₂. To improve the accuracy of basin-scale pCO₂ using satellite data, second-order MNR equations were developed and tested using satellite-derived SST and Chla data [19]. It was shown that MNR reduced the RMSE to ± 14 and $\pm 17 \mu\text{atm}$ in subtropical and subarctic regions, respectively. Further improvement was achieved by using MLR equations in North Pacific Ocean waters with SST, SSS, and Chla data as inputs, which yielded an RMSE around 17–23 μatm [17]. Later, a SOM-based approach was developed to estimate pCO₂ as a function of satellite-derived SST, SSS, MLD, and Chla data and it showed fairly good agreement with measured data in Pacific Ocean waters with an RMSE less than 20 μatm [26]. In North Atlantic Ocean waters, pCO₂ was estimated using satellite-derived SST, Chla, and MLD data with an RMSE less than 15 μatm [14], [20], [21]. Recently, an artificial neural network based on FFNN was used to estimate pCO₂ as a function of satellite-derived SST, SSS, and Chla

data in tropical Atlantic Ocean waters, where it significantly improved pCO₂ estimations within the RMSE 10 μatm [29]. In the Southern Ocean region, MLR equations were tested on satellite-derived SST and Chla data, yielding a standard deviation between 2 and 8 μatm [16]. Further improvement was achieved with an RMSE less than 7 μatm by using an FFBP approach, which estimates pCO₂ as a function of SST, Chla, latitude, and longitude in the Northern South China Sea [31]. In the river-dominated coastal and estuarine regions, PCA and MLR were used to produce pCO₂ maps from satellite-derived SST, CDOM, SSS, and Chla data [25].

Besides MLR, MNR, MPR, RFR, PCA, SOM, FFNN, and FFBP models, a quasimechanistic model was developed to estimate pCO₂ in river-dominated marginal seas in the Northwest Pacific Ocean using carbonate system parameters, such as total alkalinity (TA) and dissolved inorganic carbon (DIC). These parameters were calculated as a function of SST and Chla and used to estimate pCO₂ [35]. More recently, an MeSAA was developed to estimate pCO₂ in Eastern China Sea waters [13]. In this approach, initial pCO₂ levels were calculated due to individual underlying mechanisms, especially thermodynamic, biological, and mixing processes, which are parameterized as a function of SST, SSS, and Chla to improve the MeSAA to infer pCO₂ fields semianalytically as the summation of individual components contributed by each process. These approaches have been successfully applied to compute pCO₂ fields in regional or basin-scale oceanic domains within the errors involved in the empirical analysis and approximation solutions. However, the accurate estimation of global-scale pCO₂ changes remains a challenge owing to differences in satellite-derived and *in-situ* measured parameters as well as inadequate representation of the influencing processes and thus the seasonal and interannual pCO₂ variability. Though the global estimation of pCO₂ is possible by merging of all regional models, there is an inconsistency with the parameters used in the models and model equations that can lead to strong boundary effects across the ocean basins and latitudes. To overcome these issues, attempts have been made to construct global monthly climatological pCO₂ maps using the past decades of *in-situ* measurement data after excluding the intra and interannual variations and coastal regions in the analysis [8], [12], [36]. Similar improvement was achieved on the global maps of pCO₂ on 10° latitude and longitude spatial grids by calculating the spatial autocorrelation structure of pCO₂ using nearly 1.7 million *in-situ* pCO₂ observation data [37]; however, their analysis was restricted to small-scale variability only due to the coarse spatial resolution. This problem was overcome by generating global surface ocean climatological maps of fugacity of carbon dioxide (fCO₂) with 1° spatial resolution using an FFNN approach [30]. A data-driven ocean mixed layer scheme was also introduced to make global-scale estimation of pCO₂ by considering a larger *in-situ* measurement dataset despite its known limitations [7].

Recently, Liu and Xie [38] developed a statistical-based support vector regression method using satellite oceanographic data products, such as SST, SSS, and Chla. Bitting *et al.* [39] constructed monthly surface ocean pCO₂ climatology with a 1° × 1° spatial resolution using Bayesian neural network (BNN). Although global climatological pCO₂ maps were produced using

different remote sensing methods, there is uncertainty on $p\text{CO}_2$ estimation by 2–40 μatm in different ocean basins/climatic zones. Such a global-scale application requires the accurate estimation of $p\text{CO}_2$ fields by an appropriate method that accounts for all major controlling mechanisms. In the present work, a multiparametric nonlinear regression (MPNR) approach is developed to estimate basin- and global-scale surface ocean $p\text{CO}_2$ from satellite-derived SST, SSS, and Chla data. These data products become advantages over shipboard measurements for deriving $p\text{CO}_2$ fields in high space–time resolutions. The MPNR approach is parametrized using *in-situ* measurements of SST, SSS, and $p\text{CO}_2$ and corresponding satellite measurements of Chla from the global ocean. The sensitivity tests on the MPNR regression equations for $p\text{CO}_2$ estimation are carried out using independent data from both *in-situ* and satellite observations. The large-scale spatial and temporal variability of $p\text{CO}_2$ is further studied with regard to ocean temperature, chemistry, and circulation based on seasonal and monthly climatological maps at $1^\circ \times 1^\circ$ spatial resolution.

II. DATA AND METHODS

A. In-Situ Data

The *in-situ* data of direct $p\text{CO}_2$ and physical parameters (SST and SSS) in different oceanic waters were obtained from the National Oceanographic Data Center-National Oceanic and Atmospheric Administration (NOODC-NOAA).¹ It should be mentioned that these data were contributed by a number of organizations and institutes, namely Integrated Marine Observing System (IMOS), Pacific Marine Environmental Laboratory (PMEL), Atlantic Oceanographic and Meteorological Laboratory (AOML), and Ocean Indien Service d'Observation (OISO). Although the *in-situ* $p\text{CO}_2$ data are biased spatially, they are reasonably representative of tropical and subtropical domains, major gyre systems, warming and stratification conditions, mixing and dilution, fronts, and biological processes in the Atlantic, Pacific, and Southern Oceans. These regions have the higher physical and biological effects on $p\text{CO}_2$, because the $p\text{CO}_2$ relations with both SST and SSS represent changes in $p\text{CO}_2$ due to physical mixing and dilution (which governs dissolved inorganic carbon (DIC)) and that with Chla denote the influence of biological processes on $p\text{CO}_2$ variability. TA has been observed to have the positive relation with salinity. Hence, these influences of solubility (thermodynamic), dilution by fresh water, and mixing effects by upwelling, eddies and surface winds, and phytoplankton production on $p\text{CO}_2$ can be accounted for with the relation of $p\text{CO}_2$ with SST, SSS, and Chla, which would capture $p\text{CO}_2$ variability and distribution in surface ocean waters due to physical, chemical, and biological factors [2], [17], [36].

The primary and ancillary data (such as parameter, time, location, and number of measurements) used for the development of MPNR regression equations and its validation are described in Table I and II, respectively, whereas the *in-situ* measurement locations are shown in Fig. 1. For this study, the minimum global

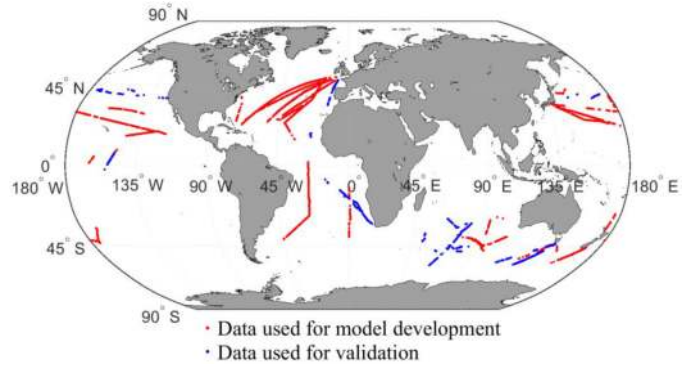


Fig. 1. Map of sample locations for the *in-situ* measured $p\text{CO}_2$ data used for deriving the multiparametric nonlinear regression equations (solid red circles) and validating the MPNR results using independent *in-situ* data (solid blue circles).

SSS is assumed as 30 PSU and the data containing the lower SSS of less than 30 PSU were excluded from the analysis. This led to approximately 57 789 *in-situ* data comprising the $p\text{CO}_2$, SST, and SSS measurements, and the corresponding Chla data were obtained from the MODIS-Aqua ocean color observations. For developing the MPNR regression equations, 40 379 measurements were used and the remaining 17 410 measurements were used for the *in-situ* and satellite model validations. Measured $p\text{CO}_2$ ranged from 296 to 488 μatm collected over the spatial domain of Atlantic, Pacific, and Southern Oceans during the periods in 2007–2018. Thus, every *in-situ* measurement dataset contains co-located $p\text{CO}_2$, SST, SSS, Chla, and ancillary data. Some data containing $f\text{CO}_2$ measurements were converted to $p\text{CO}_2$ using the following relation suggested by Takahashi *et al.* [40].

$$p\text{CO}_2 (\mu\text{atm}) = f\text{CO}_2 (\mu\text{atm}) [1.00436 - 4.669 \times 10^5 \times \text{SST} (^\circ\text{C})] \quad (1)$$

where $f\text{CO}_2$ and $p\text{CO}_2$ are used to measure the partial pressure of real and ideal gas of CO_2 in μatm , respectively, and SST in $^\circ\text{C}$.

B. Satellite Data

In order to demonstrate that the new MPNR approach is robust in deriving basin- and global-scale $p\text{CO}_2$ fields and their variability spatially and temporally, global mapped Level-3 SST and Chla products (with 4×4 km spatial resolution) from MODIS-Aqua sensor and SSS products (with $1^\circ \times 1^\circ$ resolution) from Aquarius sensor were obtained from the Goddard Space Flight Center-National Aeronautics and Space Administration (GSFC-NASA).² In addition, the Level-3 SSS (with 70×70 km spatial resolution) from Soil Moisture Active Passive (SMAP) sensor for the period 2007–2018 were obtained from the Jet Propulsion Laboratory (JPL-NASA).³ Because of the lack of *in-situ* Chla measurements corresponding to $p\text{CO}_2$ measurements, MODIS-Aqua Level-3 daily Chla with 4-km spatial resolution were used along with the *in-situ* measured $p\text{CO}_2$, SST, and SSS data for deriving MPNR parameterizations. Because there was a resolution difference between *in-situ* measurements

¹[Online]. Available: https://www.nodc.noaa.gov/oads/stewardship/data_portal.html

²[Online]. Available: <https://oceancolor.gsfc.nasa.gov>

³[Online]. Available: <https://podaac.jpl.nasa.gov/SMAP>

TABLE I
DATA USED FOR THE DEVELOPMENT OF MULTIPARAMETRIC NONLINEAR REGRESSION (MPNR) APPROACH

Region	Date	N	4-km	Latitude and Longitude	Vessel name	Observer
North Atlantic	24-29 May 2017	20286	3470	22.97N-49.30N; 8.13W-68.94W	MV Benguela Stream	U. Schuster, A.J. Watson
	7-13 July 2017					
	17-18 Aug. 2017					
	2-8 & 14-16 Sep. 2017					
North Atlantic	1-7 & 11-15 Oct. 2017	4312	729	24.50N-43.33N; 25.17W-52.26W	MV Benguela Stream	U. Schuster, A.J. Watson
	30 Apr. 2016					
	1-3 May. 2016					
Atlantic Ocean	11-13 Dec. 2016	1041	864	41.39S-49.56N; 8.84W-44.40W	RRS James Cook	V. Kitidis
	12-26 & 30-31 Oct. 2012 01-13 Nov. 2012					
North Pacific	24-29 Jan. 2017	2429	2424	16.55N-38.45N; 179.98W-179.73E	New Century 2	S. Nakaoka
	6-8 Feb. 2017					
	18-21 & 27-31 Mar. 2017					
	1 & 12-14 Apr. 2017					
South Atlantic	3-5,15-25 & 27-28 May 2017	2823	271	40.08S-12.55S; 0.89E-1.83E	R/V Ron Brown	K. Sullivan, R. Wanninkhof
	01-06 Apr. 2010 21-30 Mar. 2010					
Pacific Ocean	9-11 Oct. 2007	471	172	35.63S-42.69N; 144.54E-179.03E	R/V Mirai	A. Murata
	3-6 Nov. 2007 18-23 Dec. 2007					
Pacific Ocean	26 Apr. 2016	2412	200	35.12S-46.08S; 179.99W-179.99E	Investigator	B. Tilbrook
	23-24 & 27-31 May 2016 1-2 June 2016					
Southern Ocean	27 Apr. 2016	480	99	42.24S-47.95S; 176.70W-151.45E	IMOS/Investigator	B. Tilbrook
	23-24 & 28 May 2016					
Southern Ocean	11-15 Jan. 2016	1498	216	44.29S-52.63S; 128.02E-145.90E	R/V Aurora Australis	B. Tilbrook, J. Akl & C. Neill
	9-20,22 & 24-31 Jan. 2009					
Southern Ocean	1 & 6-9 Feb. 2009	2766	914	39.03S-48.03S; 75.82E-110E	OISO/Marion Dufresne	N. Metzl
	4-7 Feb. 2007					
Pacific Ocean	25-26 Oct. 2016	915	259	1.17N-8.80N; 164.95W-147.49W	PMEL/Cap Blanche	C.E. Cosca, S.R. Alin & R.A. Feely
	23 Jan. 2017					

TABLE II
DATA USED FOR THE MPNR VALIDATION

Region	Date	N	1°	Latitude and Longitude	Vessel name	Observer
Southern Ocean	29-30 Jan. 2015	3946	40	44S-56.05S; 112.92E-146.95E	IMOS/Aurora Australis	B. Tilbrook
	1-2 Feb. 2015					
	29-31 Mar. 2015					
	1-2 Apr. 2015					
Southern Ocean	28 & 30 Jan. 2012	2052	69	56.50S-30.00S; 52.46E-86.28E	OISO/Marion Dufresne	N. Metzl
	8-12, 17-18, 20-22 & 28-29 Feb. 2012					
Atlantic Ocean	1-3 & 5-7 Mar. 2012	10243	68	32.76S-47.90N; 24.285W-16.64E	Polarstern	S. Van Heuvan
	9-15 Mar. 2014 28-31 Oct. 2014					
South Pacific	6,18,21 & 23-27 Nov. 2014 15,17,21,27 & 29-30 Apr. 2014	356	36	37.52N-44.19N; 175.10W-178.96E	New Century 2	S. Nakaoka
	1-3,6-7 & 20-21 May 2014					
Pacific Ocean	8-10 May 2018	813	25	2.32S-6.90N; 154.95W-148.86W	PMEL/ Cap Balanche	C.E. Cosca, S.R. Alin & R.A. Feely
	5-6 July 2018					
	31 Aug. 2018					

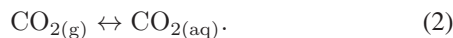
and satellite observations, the *in-situ* measured SST, SSS, and pCO₂ values within 4 km spatial resolution pixel were averaged corresponding to satellite-derived Chl_a data.

The SeaWiFS Data Analysis System (SeaDAS) was used to process the MODIS-Aqua data and establish the matchup datasets for further analysis. In order to validate the satellite-derived pCO₂ data with the *in-situ* observations in various oceanic regimes, we used the daily MODIS-Aqua Level-3 SST and Chl_a data (with 4 × 4 km resolution) and the corresponding Aquarius 7-day composite SSS data (with 1° × 1° resolution). Since the daily Aquarius Level-3 SSS products had a number of missing data lines due to the low temporal resolution, seven-day composite binned images of Aquarius SSS products were used for this analysis. Because there were differences in spatial resolution of the Level-3 MODIS-Aqua SST/Chl_a products (4 km) and Aquarius SSS products (1° degree), the MODIS-Aqua products were resampled according to the Aquarius products based on the nearest neighborhood method. Finally, the MPNR regression equations were applied on the satellite-derived products SST, SSS, and Chl_a (with 1° × 1° resolution) and produced global pCO₂ maps (with 1° × 1° resolution). For consistency, all *in-situ* pCO₂ inside each satellite pixel (with 1° × 1° resolution) were averaged so that the process of co-location is straightforward and the satellite-derived pCO₂ are better compared with *in-situ* pCO₂ data with minimal uncertainty. To illustrate the spatial and temporal variability of pCO₂, the MPNR was applied on seasonal and monthly global mapped Level-3 (satellite-derived) SST, SSS, and Chl_a data to derive the global surface ocean pCO₂ maps.

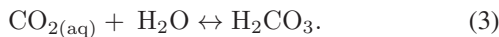
C. Model Description

1) *Theoretical Background and Model Formulation:* Atmospheric CO₂ interacts more with surface oceanic waters giving rise to the organic and inorganic forms of carbon content, which eventually leads to changes in the carbonate chemistry of ocean waters. Consequently, the ocean chemistry changes cause a reduction in the efficiency of ocean CO₂ sink and affect the marine ecosystem. Thus, the carbonate chemistry plays a vital role in the pCO₂ estimation. The governing chemical processes in ocean waters due to the atmospheric CO₂ are described below.

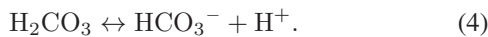
The atmospheric CO₂ interacts with surface ocean water, dissolves in it, and gives to the aqueous CO₂



The aqueous CO_{2(aq)} in (2) reacts with ocean water and results in the unstable form of carbonic acid (H₂CO₃)



The carbonic acid in (3) is a weak and unstable molecule, and it dissociates rapidly and forms bicarbonate ions (HCO₃⁻) and releases H⁺ ions



The bicarbonates in (4) again dissociate immediately and produce carbonate ions (CO₃²⁻) along with H⁺ ions

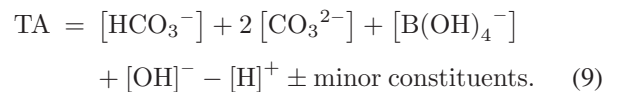
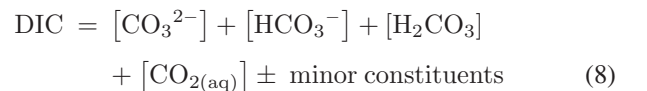


The carbonate ions in (5) further react with calcium (Ca²⁺) ions in ocean waters and produce the calcium carbonate shells (CaCO₃).



pH in ocean water, defined as the negative logarithm of H⁺ ions concentration as given in (7), increases the H⁺ ions concentration, leading to a decrease in pH value and vice versa. (4) and (5) give the increased H⁺ ions concentration in ocean waters, leading to a decrease in the pH value, which causes ocean acidification that subsequently reduces the metabolic rates, immune response of the organisms, and effects the carbonate shells/coral reefs [41]. More the CO₂ in the ocean, more the H⁺ ions released in the aquatic system, which subsequently leads to a decrease in the pH levels.

All the organic and inorganic chemical changes that occur in oceanic waters are primarily governed by the two marine carbonate chemical parameters, such as TA and DIC, which play a crucial role in understanding the influence of anthropogenic CO₂ in the ocean. The major processes that control the variation of TA and DIC in oceanic waters are biological activities (production and respiration), physical mechanisms (vertical mixing and gas exchange at the air–sea interface), and chemical processes (carbonate precipitation and dissolution). Phytoplankton photosynthesizes removing DIC and slightly increases TA in sunlight surface water, whereas cellular respiration adds DIC and slightly removes TA in dark subsurface waters. Calcification removes TA and DIC in most of sunlight available surface waters, while carbonate dissolution adds TA and DIC mostly in subsurface oceanic waters. Accurate estimation of these parameters is crucial to the precise estimation of surface ocean pCO₂. Note that the carbonate chemistry of ocean water is often described in the form of DIC, which is the sum of carbonate (CO₃²⁻), bicarbonate (HCO₃⁻), carbonic acid (H₂CO₃), aqueous CO₂ and other minor constituents, and TA, which is the sum of carbonate species and free H⁺ and OH⁻ ions.



The relative abundance of these carbon compounds is governed by the pH of the seawater, while the total amount is controlled by a much more complicated set of factors, such as biological activities (production and respiration), vertical mixing, and temperature (solubility by thermodynamic effects) [17]. To make accurate estimations of DIC in surface oceanic waters, the scheme requires additional measurements for the carbonate chemistry parameters as well as the knowledge of the carbonate dissociation constants, which are difficult to obtain accurately over the spatial and temporal scales across the latitudes with different physical and biological mechanisms (governed by evaporation–precipitation, water balance, upwelling/eddies, vertical mixing, biological production, and decomposition). It

should be noted that DIC changes in surface ocean waters are mainly controlled by the changes in SST, SSS, and Chla [17], [42]; hence, distinct and significant seasonal correlations of DIC with SST, SSS, and Chla have been found in the North Pacific Ocean [17] and Arabian Sea [42]. DIC changes can be described as a function of each influencing parameter SST, SSS, and Chla as

$$\text{DIC} = f(\text{SST}, \text{SSS}, \text{Chla}). \quad (10)$$

Owing to the influence of these parameters on surface DIC and hence pCO₂ in North Pacific waters, a multiparameter MLR approach was used to estimate the basin-scale distribution of DIC as a function of SST, SSS, and Chla [17]

$$\text{DIC} = -\text{PSST} + \text{QSSS} - \text{RChla} + \text{S}. \quad (11)$$

The pCO₂ change in surface ocean waters is also regulated by changes in TA, which is regulated by common physical and biological processes and influences the changes in pH. The TA distribution in surface ocean waters is determined by concentrations of carbonate system species, such as carbonate, bicarbonate, and boron compounds, and is due primarily to the SSS changes [43]. In various oceanographic regimes, TA displayed strong positive relations with SSS with little or no significant differences in slope between these two parameters with space and time, for different ranges of SST [17], [42]. Thus, surface ocean TA can be easily estimated as a function of SSS.

$$\text{TA} = f(\text{SSS}). \quad (12)$$

According to, [17], [36], [42], and [44], TA is computed from the first-order linear regression equation using SSS

$$\text{TA} = \text{USSS} + \text{V}. \quad (13)$$

The surface ocean pCO₂ is correlated to the difference between DIC and TA [45]

$$\text{pCO}_2 = \text{Y}(2\text{DIC} - \text{TA}) + \text{Z}. \quad (14)$$

Substituting (11) and (13) in (14), we can obtain

$$\begin{aligned} \text{pCO}_2 &= \text{Y}(2(-\text{PSST} + \text{QSSS} - \text{RChla} + \text{S}) \\ &\quad - (\text{USSS} + \text{V})) + \text{Z} \\ \text{pCO}_2 &= -2\text{PYSSS} + 2\text{QYSSS} - 2\text{RYChla} + 2\text{SY} \\ &\quad - \text{UYSSS} - \text{VY} + \text{Z} \\ \text{pCO}_2 &= -2\text{PYSSS} + (2\text{QY} - \text{UY})\text{SSS} - 2\text{RYChla} \\ &\quad + (2\text{SY} - \text{VY} + \text{Z}). \end{aligned} \quad (15)$$

Considering $A = -2\text{PY}$, $B = (2\text{QY} - \text{UY})$, $C = -2\text{RY}$, and $D = (2\text{SY} - \text{VY} + \text{Z})$ and substituting in (15), we can obtain

$$\text{pCO}_2 = \text{ASST} + \text{BSSS} + \text{CChla} + \text{D} \quad (16)$$

where P–S, U–V, Y–Z, and A–D are constants for (11), (13), (14), and (16), respectively, and are obtained using regression analysis. Using (11) and (13), surface ocean DIC and TA can be calculated from SST, SSS, and Chla. (14) is essentially a thermodynamic equation for the estimation of pCO₂ from TA and DIC values. Estimation of pCO₂ from (14) using chemical parameters DIC (SST, SSS, and Chla) and TA (SSS) can lead to

a large uncertainty because of the large seasonal and interannual variability (caused by physical and biological processes) or propagation of errors associated with the calculation of DIC and TA as a function of biophysical parameters (SST, SSS, and Chla) using (11) and (13). Computation using a straightforward MPNR approach derived in this study (16) gives an accurate estimation of basin- and global-scale pCO₂ as strength of each influencing parameters (physical and biological) causing the changes in pCO₂ is well accounted through distinct correlations of pCO₂ with SST, SSS, and Chla.

2) *Model Parameterization*: The surface ocean pCO₂ variations are primarily influenced by SST changes caused due to the physical processes, such as solar radiation input, heat exchange between ocean to atmosphere and atmosphere to ocean, intense mixing, and mixed layer dynamics. In earlier studies, SST was considered as a single parameter or one of the dominant parameters to estimate pCO₂ [17], [18], [22], [29], [34], [38], [42], [46]. Based on the experimental studies and thermodynamic calculations, Stephen *et al.* [18] observed the effect of SST on pCO₂ and determined that every 1°C rise in SST will lead to an increase in pCO₂ by 4.23%. In other oceanic regions, there was a significant deviation of pCO₂ from their observation indicating that other parameters also play a crucial role in surface ocean pCO₂ variations. Thus, an MPNR approach is developed to estimate pCO₂ as a function of all influencing parameters that have distinct positive or negative correlations with pCO₂. Because of the rapidly changing oceanic regions and the difficulty in discerning pCO₂ trends accurately, many studies have estimated pCO₂ trends over physically and biologically defined regions using multiparameters, either derived from *in-situ* observations or from satellite observations [13], [16], [17], [19], [25], [47], [48]. In the tropical and subtropical regions of both northern and southern hemispheres, both DIC and pCO₂ are mainly influenced by thermodynamic effects and exchange processes at the air–sea interface; in polar and subpolar regions, DIC and pCO₂ are affected by biological activities and chemical factors; and in equatorial regions, the variability in DIC and pCO₂ is mainly due to thermodynamic effects, vertical/lateral mixing, and biological activities. Thermodynamic effects in oceanic waters are solely controlled by changes in SST, thus the resulting changes in SST mainly influence the pCO₂ levels. Physical mixing with subsurface waters and dilution by freshwater (e.g., linked to rain events and river discharges) are chiefly controlled by changes in SSS, thus the resulting changes in SSS mainly influence the pCO₂ levels. Significant seasonal changes in pCO₂ and DIC are regulated largely by biological activities (as accounted by Chla), deep water upwelling, and cyclonic eddies. Based on these pCO₂ variations in different oceanic regimes and the theoretical foundation presented in the earlier section, a multiparametric MPNR approach is developed to estimate spatial and temporal variations of pCO₂ for the global ocean as a function of SST, SSS, and Chla

$$\text{pCO}_2 = \text{A SST} + \text{B SSS} + \text{C log}_{10}\text{Chla} + \text{D} \quad (17)$$

where A, B, C, and D are the coefficients obtained from regression analysis using global *in-situ* pCO₂, SST, SSS, and corresponding satellite-derived Chla. Changes in phytoplankton biomass are accounted by intracellular Chla contents based on

the availability of light, nutrients, seawater physical properties, and CO₂ concentrations [49]. Diurnal variation in phytoplankton biomass and physiological state of the phytoplankton are greatly influenced by physical factors and light fluctuations, which may have a major influence on the relationship between pCO₂ and Chla. Hales *et al.* [35] suggested that a straightforward linear relationship between pCO₂ and Chla is very difficult to achieve due to these factors. Thus, biological effect on pCO₂ variation is accounted by the logarithm of Chla [$\log_{10}\text{Chla}$] in the present study. In the absence of concurrent *in-situ* Chla data, we have used MODIS-Aqua Level-3 daily binned Chla data with 4-km spatial resolution corresponding to *in-situ* pCO₂, SST, and SSS data measured in diverse oceanic waters. The *in-situ* data were collected from Pacific, Atlantic, and Southern Ocean waters by various research teams across the world and contributed to the NODC-NOAA database for calibration and validation purposes. Although the data contained a large number of sampled pCO₂, SST, and SSS, some data were excluded from the analysis when global ocean SSS < 30 PSU, consistent with the previous studies [17], due to anomalous physical processes where these samples were collected [2]. This led to a total of 57 789 data points used in this study for the parameterization and validation of the MPNR approach. Of these, 40 379 were used for MPNR parameterization and the remaining 17 410 samples were used for the *in-situ* and satellite validations. *In-situ* measured pCO₂, SST, and SSS data were continuous, whereas Chla were derived from satellite data with 4-km spatial resolution. To avoid spatial resolution inconsistencies between *in-situ* and satellite data, 40 379 *in-situ* data which is used for MPNR parameterization were resampled by averaging the values over square cells of 4-km size so as to be consistent with the Chla data. This led to a total of 10 000 *in-situ* and satellite-derived measurements of the same spatial resolution.

Based on the global *in-situ* measurements of pCO₂, SST, and SSS and the corresponding satellite-derived Chla obtained from various oceanic regions, it was observed that most of the pCO₂ data showed negative correlation with SST, SSS, and Chla in polar and subpolar regions; widespread pCO₂ data showed strong positive correlation with SST and SSS data and negative correlation with Chla data in tropical and subtropical regions; and the remaining pCO₂ data displayed negative correlation with SST and positive correlation with SSS and Chla in equatorial regions. Fig. 2 shows all the global observed trends in surface ocean pCO₂ with respect to the SST, SSS, and Chla data. Based on the observed global trends of pCO₂ with respect to independent parameters such as SST, SSS, and Chla, our findings revealed that the same parameter exhibited different trends with respect to pCO₂ variability in different oceanic regimes. Because of these complex and rapidly changing trends in different oceanic regimes, no single model reported previously was capable of discerning global-scale pCO₂ trends specifically on spatial and longtime scales when pCO₂ has different, significant trends with the individual parameter mentioned previously. To overcome this problem, we parameterized our MPNR approach with respect to specific ranges of SST and SSS (according to the global trends) using the first-order multiple nonlinear regression equations. For example, the specific ranges of SST (SST < 15, 15 ≤ SST < 26, and SST ≥ 26) and SSS (30 < SSS ≤ 34.9

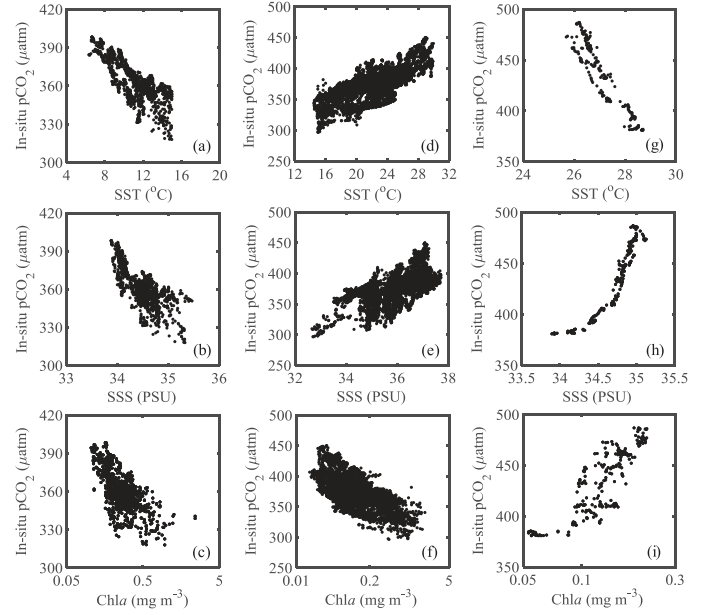


Fig. 2. Scatterplots of the relationships of pCO₂ with sea surface temperature (SST), sea surface salinity (SSS), and chlorophyll-*a* (Chla) concentration for the (a–c) MPNR-1, (d–f) MPNR-2, and (g–i) MPNR-3 based on the variations of pCO₂ with respect to the physical oceanographic conditions (SST and SSS).

and SSS > 34.9) were considered. Fig. 3 shows the MPNR architecture based on SST and SSS conditions.

Because the available 40 379 *in-situ* pCO₂ and other data were randomly distributed spatially and temporally, these data were separated and regrouped according to the SST and SSS conditions following the observed global trends of pCO₂ with respect to SST, SSS, and Chla data. After regrouping of the data, 5151 data were used for the MPNR-1 analysis, 34 313 for the MPNR-2 analysis, and 915 data for the MPNR-3 analysis. The available data were co-located corresponding to the satellite 4-km spatial resolution Chla data, which resulted 1502, 8239, and 259 data points for the MPNR-1, MPNR-2, and MPNR-3 analyses, respectively.

MPNR-1:

$$\text{pCO}_2 = -3.4646\text{SST} - 5.1624\text{SSS} - 37.3073\log_{10}\text{Chla} + 548(\text{SST} < 15, \text{N} = 1502) \quad (18)$$

MPNR-2:

$$\text{pCO}_2 = 2.6544\text{SST} + 10.5464\text{SSS} - 22.41\log_{10}\text{Chla} - 73 (15 \leq \text{SST} < 26, \text{SST} > 26, \text{and SSS} > 34.9, \text{N} = 8239) \quad (19)$$

MPNR-3:

$$\text{pCO}_2 = -29.8310\text{SST} + 0.8431\text{SSS} + 48.4430\log_{10}\text{Chla} + 1297(\text{SST} \geq 26 \text{ and SSS} \leq 34.9, \text{N} = 259). \quad (20)$$

Using the multiparametric and multiple regression analyses of pCO₂ with respect to SST, SSS, and Chla data based on the SST and SSS conditions (Fig. 3), the new MPNR was derived that serves as an accurate estimator of global-scale pCO₂ from satellite observation data.

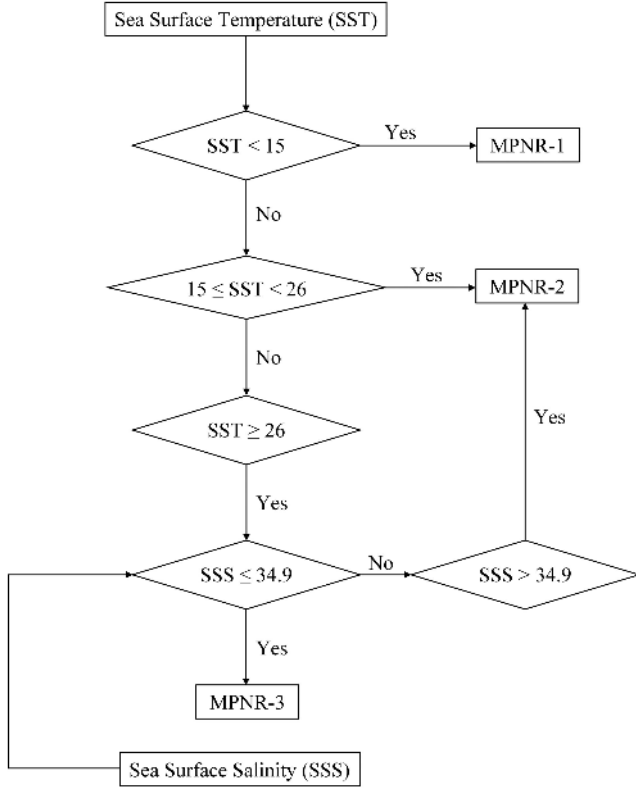


Fig. 3. Flowchart showing the architecture of MPNR based on the SST and SSS conditions.

III. PERFORMANCE ASSESSMENT

Quantitative performance assessment of the MPNR approach is made based on the standard statistical matrices, such as mean relative error (MRE), mean normalized bias (MNB), root-mean-square error (RMSE), correlation coefficient (R^2), slope, and intercept. The MRE, MNB and RMSE matrices are defined as,

$$\text{MRE} = \frac{1}{N} \sum_{i=0}^N \frac{|(\text{pCO}_2^{\text{estimated}} - \text{pCO}_2^{\text{in-situ}})|}{\text{pCO}_2^{\text{in-situ}}} \quad (21)$$

$$\text{MNB} = \frac{\sum_{i=0}^N (\text{pCO}_2^{\text{estimated}} - \text{pCO}_2^{\text{in-situ}})}{N} \quad (22)$$

$$\text{RMSE} = \sqrt{\frac{\sum_{i=0}^N (\text{pCO}_2^{\text{estimated}} - \text{pCO}_2^{\text{in-situ}})^2}{N}} \quad (23)$$

whereas the slope, intercept, and R^2 are calculated from regression analysis between the estimated ($\text{pCO}_2^{\text{estimated}}$) and measured *in-situ* ($\text{pCO}_2^{\text{in-situ}}$) pCO_2 values. The MRE and RMSE matrices give the systematic and random errors, respectively, whereas the MNB, intercept, slope, and R^2 are used in conjugation with other matrices to examine deviations of the estimated pCO_2 values from the measured *in-situ* pCO_2 values.

IV. RESULTS AND DISCUSSION

This section presents validation results using independent *in-situ* data and satellite matchup data and the spatial distribution and temporal variability of basin- and global-scale pCO_2 using

satellite oceanographic data. The *in-situ* and satellite validation are performed using independent data obtained along several cruise tracks in the Pacific, Atlantic, and Southern Oceans over the period of 2012, 2014, 2015, and 2018 spanning from January to November. Several test cases using satellite oceanographic data from the regional and global ocean regimes were carried out to detect changes in pCO_2 fields due to the dominance of heating, cooling, mixing, and biological effects as previously reported with the extensive climatological data.

A. Validation of the Estimated pCO_2 With In-Situ (Direct and Derived) pCO_2 Data

The *in-situ* validation dataset contains simultaneous measurements of pCO_2 , SST, and SSS with the exception of the Chla data. Thus, the daily Level-3 MODIS-Aqua-derived Chla data were obtained corresponding to the *in-situ* pCO_2 , SST, and SSS data. In total, 17 410 independent *in-situ* data have measured pCO_2 , SST, and SSS data and satellite-derived Chla data. For the purpose of *in-situ* and satellite matchup analysis, the *in-situ* data were converted to the same grid with $1^\circ \times 1^\circ$ spatial resolution data provided by the satellite sensors. This resulted in a total of 238 sets in the same samples. These data were then regrouped based on the SST and SSS conditions, and accordingly, the estimated values (SST, SSS, and pCO_2) were compared with the *in-situ* measured values. Since pCO_2 is dependent on SST, SSS, and Chla fields, the daily Level-3 SST and SSS fields derived from the satellite data (MODIS-Aqua, Aquarius, and SMAP) were compared with measured *in-situ* data (such a comparison is not presented for Chla because of the absence of data). Fig. 4 (a, e, i, and m) shows that the satellite-derived SST values are in good agreement with the measured values with low errors for SST (MRE 0.026, RMSE 0.65, MNB -0.07) and high slope and correlation coefficients (Slope 1, R^2 0.99). Similarly, Fig. 4 (b, f, j, and n) shows the satellite-derived SSS values are consistent with the measured SSS values with small errors (MRE 0.004, RMSE 0.22, MNB 0.006) and high slope and correlation coefficients (Slope 0.93, R^2 0.94).

Slight underestimation of SSS at the lower end of the range and overestimation of SSS at the intermediate and higher ends of the range may be caused by diurnal SSS variations [50], [51] and differences due to pixel measurements by satellites and spot measurements by *in-situ* observations. However, the validation results indicate that the estimated SST and SSS are consistent with those based on the *in-situ* measurements within acceptable errors in the context of satellite data analysis, which ensures that the pCO_2 fields can be estimated reliably using the satellite-derived products of SST, SSS, and Chla fields. Fig. 4 (c, g, k, and o) shows the comparison of estimated pCO_2 with independent measurement data (SST, SSS, and Chla) in the Atlantic, Pacific, and Southern Oceans. This validation analysis yielded small errors and high correlation coefficients (MRE 0.010, RMSE 5.35, MNB 0.049, Slope 0.94, and R^2 0.90 for the cases of waters with $\text{SST} < 15$; MRE 0.019, RMSE 8.48, MNB 0.69, Slope 0.72, and R^2 0.86 for the cases of waters with $15 \leq \text{SST} < 26$, $\text{SST} > 26$, and $\text{SSS} > 34.9$; and MRE 0.010, RMSE 5.41, MNB 1.68, Slope 1.00, and R^2 0.91 for the cases of waters with $\text{SST} \geq 26$ and $\text{SSS} \leq 34.9$). The overall

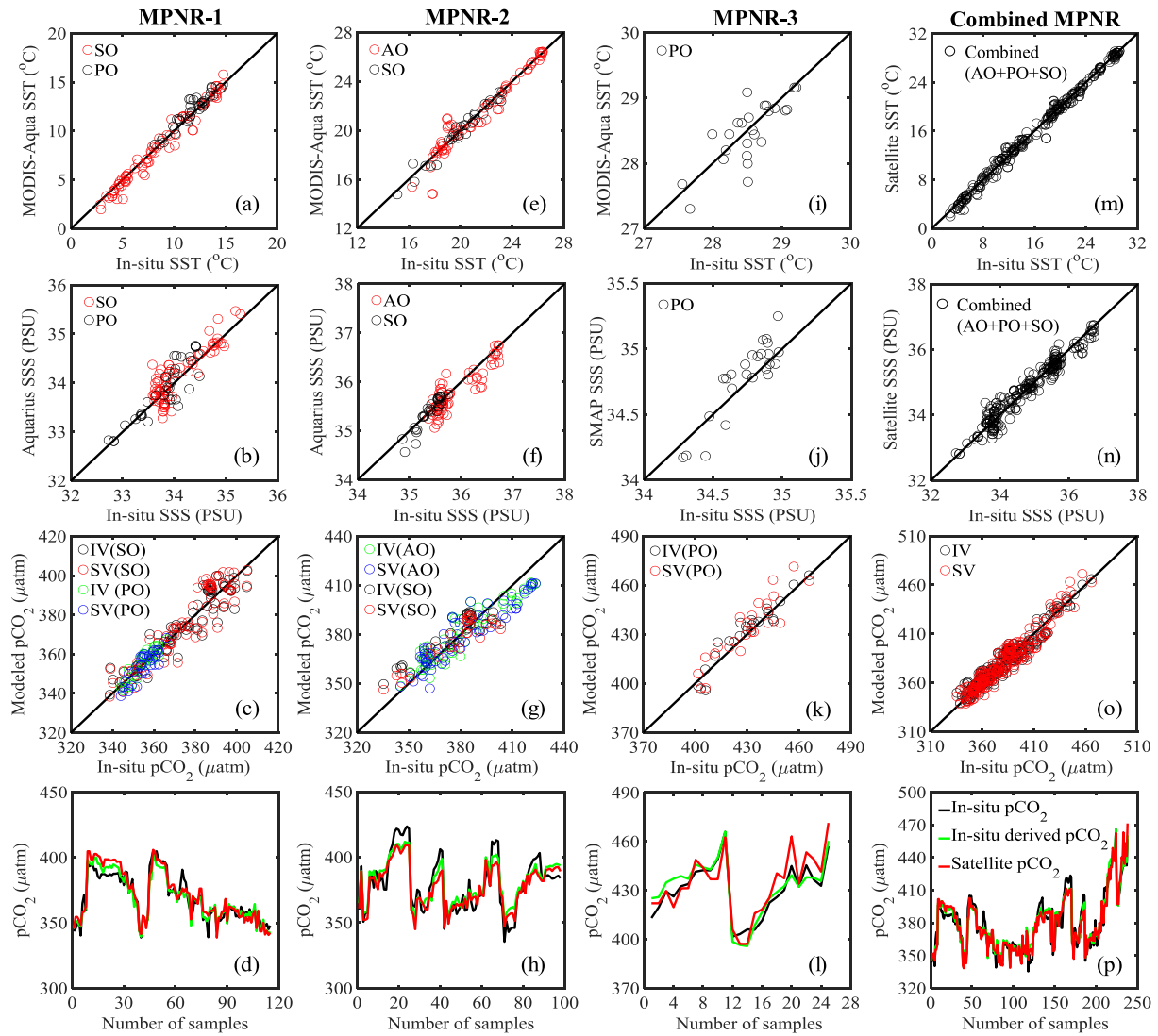


Fig. 4. Scatterplots (first three rows) and line plots (fourth row) showing the comparison of estimated SST, SSS, and $p\text{CO}_2$ with the measured values in the Pacific Ocean (PO), Atlantic Ocean (AO), and Southern Ocean (SO). IV – *In-situ* validation results; SV – Satellite validation results; MPNR-1, MPNR-2, and MPNR-3 are the validation results based on the three SST and SSS conditions. The combined MPNR represents the overall validation results in PO, AO, and SO waters. Because of the absence of *in-situ* Chla data, a similar validation at the $p\text{CO}_2$ sampling locations could not be performed.

performance of the MPM for the entire ranges of SST, SSS, and Chla in different oceanic regimes is also exceptionally good (MRE 0.014, RMSE 6.68, MNB 0.48, Slope 0.92, and R^2 0.93), which indicates the robustness of the MPNR approach for global-scale applications.

B. Validation of the Satellite $p\text{CO}_2$ With *In-Situ* Data

To validate the satellite-derived $p\text{CO}_2$ data with the *in-situ* observations, the MPNR regression equations were applied on satellite data products (SST, SSS, and Chla) to produce daily $p\text{CO}_2$ products in areas where independent *in-situ* $p\text{CO}_2$ data were available along ship transects in the Atlantic, Pacific, and Southern Oceans. In total, 17 410 *in-situ* measured $p\text{CO}_2$, SST, and SSS and satellite-derived Chla data were used for the satellite validation. For the purpose of *in-situ* and satellite matchup analysis, the *in-situ* data were converted to the same grid with $1^\circ \times 1^\circ$ spatial resolution data provided by the satellite

sensors. This resulted in a total of 238 *in-situ* measured $p\text{CO}_2$, SST, and SSS and satellite-derived Chla data. Of these, 115 samples from Southern and Pacific Ocean waters were used for validating the MPNR-1, 98 samples from Atlantic and Southern Ocean waters for validating the MPNR-2, and 25 samples from Pacific Ocean waters for validating the MPNR-3. Fig. 4 (c, g, k, and o) shows a comparison of the *in-situ* measured $p\text{CO}_2$ with those derived from satellite data (red circles in scatterplots and red lines in line plots) in various oceanic regimes, including the Atlantic, Pacific, and Southern Oceans. Consistent with the *in-situ* validation results, the MPNR reproduced *in-situ* measured $p\text{CO}_2$ values with the MRE 0.012, RMSE 6.12, MNB -0.10 , Slope 1, and R^2 0.89 for the cases of waters with $\text{SST} < 15$; MRE 0.019, RMSE 8.77, MNB -0.29 , Slope 0.72, and R^2 0.84 for the cases of waters with $15 \leq \text{SST} < 26$, $\text{SST} > 26$, and $\text{SSS} > 34.9$; and MRE 0.016, RMSE 8.45, MNB 3.36, Slope 1.02, and R^2 0.82 for the cases of waters with $\text{SST} \geq 26$ and $\text{SSS} \leq 34.9$. The overall agreement of satellite-derived $p\text{CO}_2$

TABLE III
STATISTICS OF *IN-SITU* AND SATELLITE DERIVED PCO₂ VALIDATION DATA

MPNR	Validation	MRE	MNB	RMSE	SLOPE	R ²	N
MPNR-1	In-situ	0.010	0.049	5.35	0.94	0.90	115
	Satellite	0.012	-0.10	6.12	1.00	0.89	
MPNR-2	In-situ	0.019	0.69	8.48	0.72	0.86	98
	Satellite	0.019	-0.29	8.77	0.72	0.84	
MPNR-3	In-situ	0.010	1.68	5.41	1.00	0.91	25
	Satellite	0.016	3.36	8.45	1.02	0.82	
All data	In-situ	0.014	0.48	6.68	0.92	0.93	238
	Satellite	0.016	0.18	7.56	0.95	0.91	

with *in-situ* measured pCO₂ data collected in different oceanic regimes during different periods was good (MRE 0.016, RMSE 7.56, MNB 0.18, Slope 0.95, and R² 0.91). The mean absolute differences in satellite-derived and *in-situ* measured pCO₂ were 4.82 μatm for the cases of waters with SST < 15, 7.46 μatm for the cases of waters with 15 ≤ SST < 26, SST > 26, and SSS > 34.9, 7.08 μatm for the cases of waters with SST ≥ 26 and SSS ≤ 34.9, and 6.14 μatm for the entire validation data. Slight differences were still observed across some samples due to differences in SST, SSS, and Chla between *in-situ* measured and satellite-derived data, pixel and spot measurements, and influx and mixing of the waters under different sea state conditions and continental effects. Table III shows the statistics of *in-situ* and satellite validations.

C. Comparison With the Regional Models

The space-time variability of pCO₂ in different ocean basins across the latitudes has been previously reported by several studies. For instance, in the northern Pacific Ocean, Stephens *et al.* [18] estimated pCO₂ from the MPR model as a function of SST and longitude with an RMSE value of ±17 and ±40 μatm in tropical and subpolar region. Ono *et al.* [19] applied the second-order MNR equations to satellite-derived SST and Chla data to produce pCO₂ which yielded an RMSE value of ±14 and ±17 μatm in subtropical and subarctic regions. Sarma *et al.* [17] estimated pCO₂ from the MLR model using satellite-derived SST, SSS, and Chla products in North Pacific Ocean waters, which yielded an RMSE of 17–23 μatm. Nakaoka *et al.* [26] estimated pCO₂ from the SOM as a function of SST, SSS, Chla and Julian day in Northern Pacific Ocean waters with an RMSE value of 17–20.2 μatm. In Atlantic Ocean regimes, Jamet *et al.* [14] used the MLR to estimate pCO₂ as a function of SST, SSS, and MLD, which produced an RMSE value of 8.98–15.01 μatm. Chierici *et al.* [21] developed the MPR equations that estimates pCO₂ as a function of SST, Chla, and MLD for Northern Atlantic Ocean waters with an RMSE value of 10.8 μatm. Telszewski *et al.* [20] developed and tested an SOM approach using the satellite-derived SST, Chla, and MLD products in North Atlantic regions, which resulted an RMSE of 11.6 μatm. Friedrich and

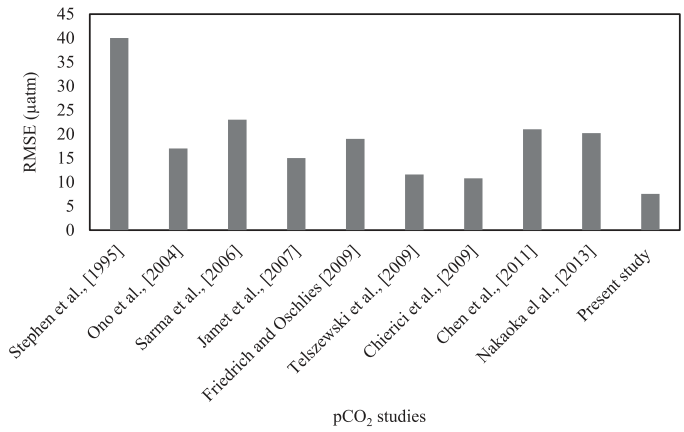


Fig. 5. Bar graph showing the comparison of the RMSE of the present study with the regional pCO₂ studies.

Oschlies [28] developed a KFM to estimate pCO₂ in North Atlantic Ocean waters as a function of SST and Chla. This model yielded an RMSE value of 19 μatm. Chen *et al.* [48] developed and tested an MLR model in Southern Atlantic and Indian Ocean waters, which yielded an RMSE of 21 μatm. Compared to these regional studies in Pacific, Atlantic, and Southern Oceans, the MPNR estimated pCO₂ trends in close agreement with measured values with an RMSE of 6.68 and 7.56 μatm for *in-situ* and satellite validation results, respectively. While the *in-situ* data exhibited discontinuous pCO₂ trends in different basins, satellite products derived from the MPNR captured sharp space–time variations of pCO₂ trends in global oceanic waters caused by various physical and biological processes. Fig. 5 shows the RMSE of the present study compared with the regional pCO₂ studies.

D. Basin- and Global-Scale pCO₂ Fields

1) *Individual Effects of SST, SSS, and Chla on the Global pCO₂ Variations*: Estimation of the basin- and global-scale pCO₂ fields on the monthly and seasonal time scales is important for understanding the time–space variability for the air–sea CO₂ exchange in different ocean basins and quantify its effects on the future global climate [8], [14]. Because spatial and temporal variations of surface ocean pCO₂ are influenced by three easily measurable parameters SST, SSS, and Chla (as controlled by physical and biogeochemical processes, such as biological production or respiration, physical mixing, ocean currents, and circulations), the monthly averaged global satellite images of SST, SSS, Chla, and pCO₂ data (1° × 1° resolution) during the period January–December 2014 are examined to capture their seasonal, regional, and global trends (Figs. 7–10).

This period was considered for two reasons: more independent *in-situ* pCO₂ validation data (approximately 10 599) and availability of *in-situ* and satellite-based climatological pCO₂ maps for the reference year 2014 [36]. Fig. 6 shows the MPNR implementation using the satellite-derived data products (SST, SSS, and Chla). Among the three influencing parameters, SST changes are observed to have the dominant effect on pCO₂ due to direct solar heating, physical mixing, ocean

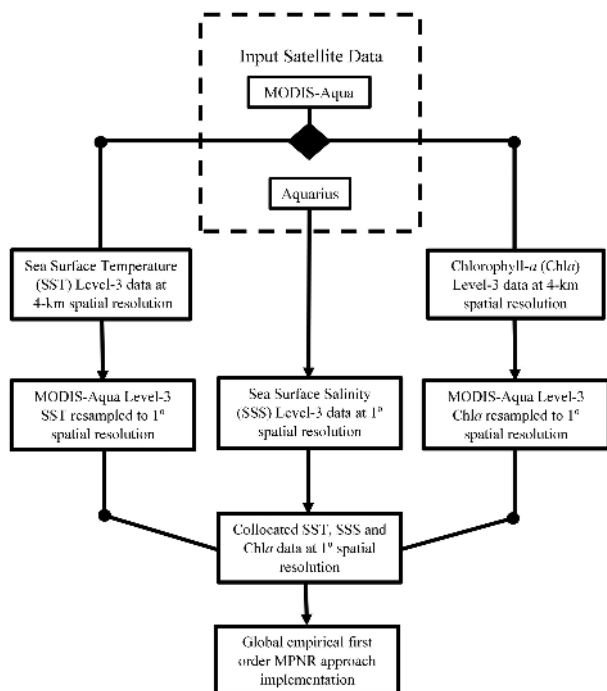


Fig. 6. Flowchart showing the implementation of multiparametric model (MPNR) using satellite oceanographic data in global oceanic waters.

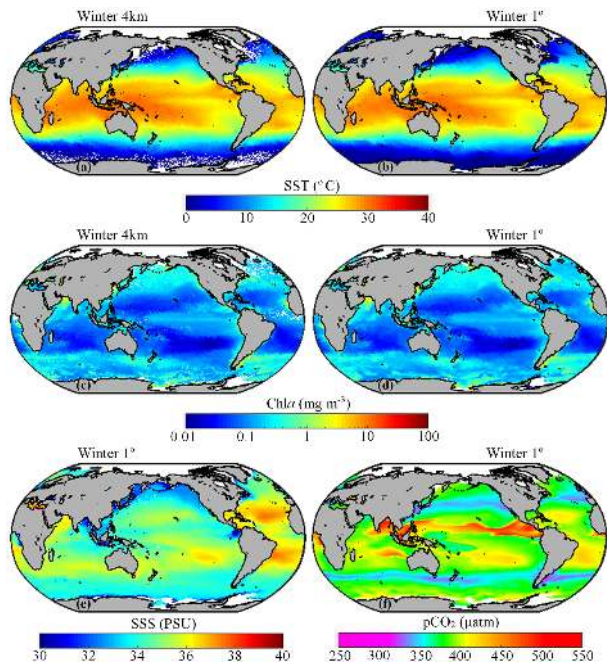


Fig. 7. Global maps of (a and b) MODIS-Aqua Level-3 data of SST at 4-km and $1^\circ \times 1^\circ$ spatial resolution, (c and d) MODIS-Aqua Level-3 data of Chl at 4-km and $1^\circ \times 1^\circ$ spatial resolution, (e) Aquarius Level-3 SSS data at $1^\circ \times 1^\circ$ spatial resolution, and (f) pCO₂ data at $1^\circ \times 1^\circ$ spatial resolution for the winter season (January–March) of 2014.

currents/circulations, heat exchange between the ocean and atmosphere, and bottom boundary atmospheric effects. Fig. 11(a) shows the monthly global images of SST ($1^\circ \times 1^\circ$ resolution) during the period from January to December 2014. The tropical and subtropical band (45°N – 45°S) exhibits large SST values

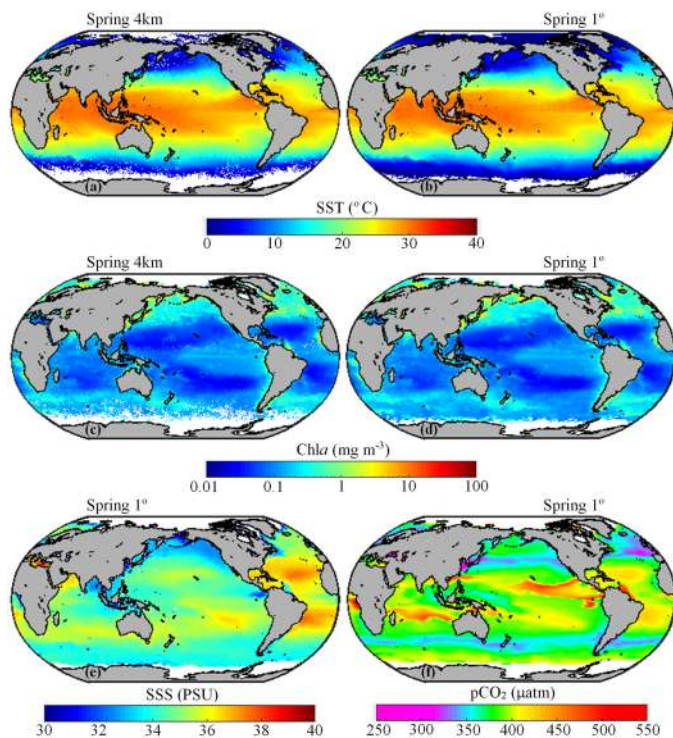


Fig. 8. Global maps of (a and b) MODIS-Aqua Level-3 data of SST at 4-km and $1^\circ \times 1^\circ$ spatial resolution, (c and d) MODIS-Aqua Level-3 data of Chl at 4-km and $1^\circ \times 1^\circ$ spatial resolution, (e) Aquarius Level-3 SSS data at $1^\circ \times 1^\circ$ spatial resolution, and (f) pCO₂ data at $1^\circ \times 1^\circ$ spatial resolution for the spring season (April–June) of 2014.

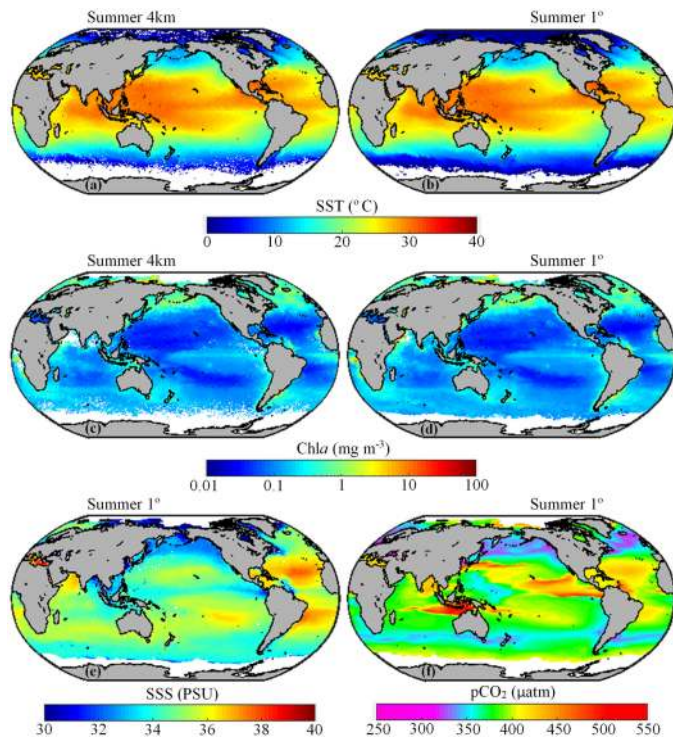


Fig. 9. Global maps of (a and b) MODIS-Aqua Level-3 data of SST at 4-km and $1^\circ \times 1^\circ$ spatial resolution, (c and d) MODIS-Aqua Level-3 data of Chl at 4-km and $1^\circ \times 1^\circ$ spatial resolution, (e) Aquarius Level-3 SSS data at $1^\circ \times 1^\circ$ spatial resolution, and (f) pCO₂ data at $1^\circ \times 1^\circ$ spatial resolution for the summer season (July–September) of 2014.

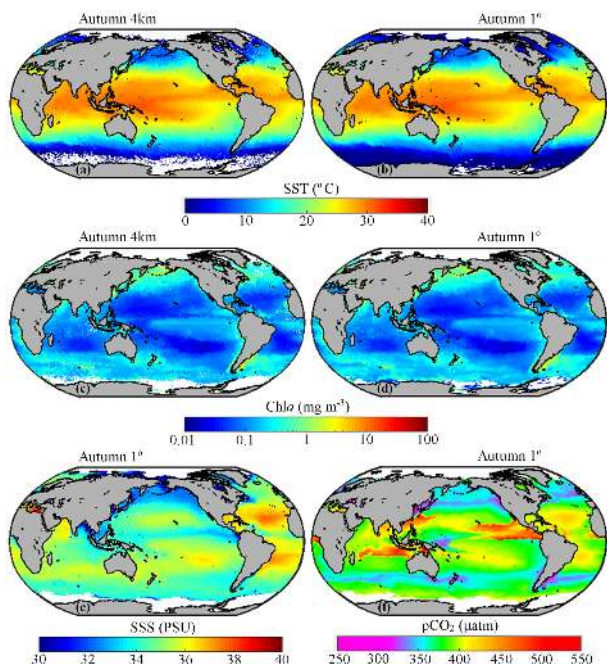


Fig. 10. Global maps of (a and b) MODIS-Aqua Level-3 data of SST at 4-km and $1^\circ \times 1^\circ$ spatial resolution, (c and d) MODIS-Aqua Level-3 data of Chla at 4-km and $1^\circ \times 1^\circ$ spatial resolution, (e) Aquarius Level-3 SSS data at $1^\circ \times 1^\circ$ spatial resolution, and (f) pCO₂ data at $1^\circ \times 1^\circ$ spatial resolution for the autumn season (October–December) of 2014.

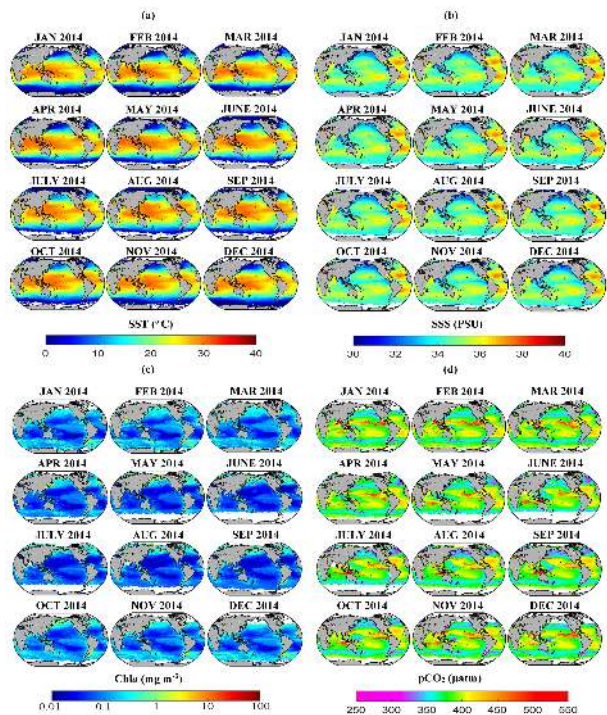


Fig. 11. Global distributions of monthly satellite-derived (a) SST, (b) SSS, (c) Chla, and (d) pCO₂ at $1^\circ \times 1^\circ$ spatial resolution.

(>15°C), whereas the northern and southern polar and subpolar band (45°–90°) exhibits small SST values (<15°C). Spatial and temporal variations of pCO₂ in tropical and subtropical bands are mainly controlled by SST variations [52]; thus, these regions are most important for the sea–air CO₂ exchange [53]–[55].

Solubility of CO₂ gas molecules in surface ocean waters is mainly controlled by SST, which decreases progressively from equator toward the poles due to differences in their distance to the sun. Because the solubility of CO₂ in surface ocean waters is inversely correlated with SST [17], [18], cold ocean waters (low SST) have higher solubility of CO₂, whereas warm ocean waters (high SST) have low solubility of CO₂. Thus, polar and subpolar bands act as a major sink for atmospheric CO₂, whereas equatorial bands (10°N–10°S) act as a major source to the atmospheric CO₂. Polar and subpolar bands of both northern and southern hemispheres have less solar radiation (low SST) and hence the solubility of CO₂ depends sensitively on the low SST bands in the polar and subpolar oceanic regions. Biological activities play a predominant role in high spatial and temporal variability of pCO₂ through the processes of photosynthesis, respiration, and calcium carbonate (CaCO₃) shell production or dissolution.

Fig. 11(c) shows the monthly global images of Chla ($1^\circ \times 1^\circ$ resolution) during the period from January to December 2014. Tropical and subtropical bands of open ocean waters show very low Chla values, whereas polar and subpolar regions show high Chla values due to the strong biological production. Seasonal variations of pCO₂ in polar and subpolar band are strongly influenced by the seasonal variations of Chla [12]. High biological production leads to a decrease in surface ocean pCO₂ through the process of photosynthesis. The polar and subpolar bands of northern hemisphere show low pCO₂ values due to the strong biological activity, but the southern polar band shows high pCO₂ values as compared to the northern polar band due to the low biological production and high solubility of CO₂. SSS is another essential parameter that controls the horizontal and vertical gradient of surface ocean pCO₂ variations caused by ocean circulation, stratification, and mixing processes (upwelling and downwelling). Upwelling of ocean water brings nutrients and CO₂-rich cold water to the surface causing changes in surface ocean pCO₂. SSS in ocean waters is mainly controlled by SST changes due to evaporation, rain events, river inflow, and melting of the ice sheets at the poles. Fig. 11(b) shows the monthly global images of SSS ($1^\circ \times 1^\circ$ resolution) during the period from January to December 2014. It is seen that the open ocean waters of tropical and subtropical regions have high SSS (>36 PSU) due to evaporation and dry offshore winds, the polar and subpolar oceanic waters have low SSS (<33 PSU) due to melting of the ice sheets and freshwater inputs from the continents, and the equatorial bands have relatively low SSS due to high precipitation and river inflow.

2) *Combined Effects of SST, SSS, and Chla on the Global pCO₂ Variations:* Stratified regions of the global ocean associated with low nutrients and Chla (stratification prevents the vertical mixing of nutrients and thus limits the biological production) and high SST and SSS exhibit high pCO₂ levels throughout the year, whereas the regions characterized by high nutrients, strong biological production (high Chla), and relatively low SST and SSS have low pCO₂ levels. In tropical and mid-latitude bands, pCO₂ is mainly controlled by changes in SST and SSS and the influence of Chla on pCO₂ is minimal. In polar and subpolar oceanic waters, pCO₂ is more influenced by Chla variations than

SST and SSS changes. In equatorial oceanic waters, changes in all three parameters SST, SSS, and Chl a have a profound role in the pCO $_2$ variations. Regions with high solubility and low Chl a have high pCO $_2$, whereas regions with high solubility and Chl a have low pCO $_2$ due to the fact that the biological productivity decreases pCO $_2$ values. Considering the global images of pCO $_2$, southern polar (60°S–90°S) bands have higher pCO $_2$ levels compared to the northern polar bands, because the enhanced biological activities (high Chl a) in northern polar regions cause a decrease in pCO $_2$ (through photosynthesis) despite the high solubility of CO $_2$ and the diminished biological production (low Chl a), and high solubility of CO $_2$ in southern polar regions cause an increase in pCO $_2$. Regardless of the seasonal variations, the transitional band between 35° and 55° in both northern and southern hemispheres exhibits low pCO $_2$ values, because of high nutrients, biological production and mixing (cooling effect) of the cold water (moving from the pole to equator), and warm water (flowing from the equator to the polar region). Eastern part of the equatorial Pacific Ocean acts as a strong upwelling region due to the movement of northeastern (NE) and southeastern (SE) trade winds toward the western side, leading to the flow of surface waters from the eastern to the western equatorial Pacific Ocean [56]. Upwelling regions bring bottom cold CO $_2$ rich waters to the surface causing an increase in pCO $_2$. As a consequence of strong upwelling in the eastern equatorial Pacific Ocean, high pCO $_2$ occurs in this region as a strong source to the atmosphere CO $_2$.

In the equatorial band (10°N–10°S), satellite pCO $_2$ levels are higher (>430 μ atm) across the western–eastern Pacific Ocean during winter (Fig. 7). Intermediate pCO $_2$ values (340–380 μ atm) are observed in the western and central equatorial Pacific Ocean during spring, summer, and autumn seasons (Figs. 8–10), and a high pCO $_2$ trend (>400 μ atm) is seen from the central equatorial Pacific Ocean to the eastern equatorial Pacific Ocean. Similar pCO $_2$ trends were observed in the monthly pCO $_2$ climatological maps produced by Takahashi *et al.* [36]. The observed pCO $_2$ values are also consistent with the discrete *in-situ* data. Seasonal variations of pCO $_2$ levels in the equatorial Pacific Ocean are owing to the profound effects of SST, SSS, and Chl a , strong upwelling (eastern equatorial Pacific Ocean), and downwelling (western equatorial Pacific Ocean) [57], which are greatly influenced by the El Niño and La Niña events.

In the subtropical band, a low pCO $_2$ structure (<335 μ atm) is observed that stretches eastward from east of northern Japan coast in the North Pacific Ocean (Figs. 7–10). The pCO $_2$ levels are slightly decreased (<300 μ atm) along the east and west coasts of Japan and America. The position of this low pCO $_2$ structure changed with the seasons; for instance, it was located between 32°N and 41°N latitudinal band during winter and spring season (Figs. 7 and 8) and between 41°N and 50°N during summer and autumn seasons (Figs. 9 and 10). The seasonal shift in low pCO $_2$ structure in the Pacific Ocean is caused by intense biological production and mixing of warm and cold ocean currents as reported previously by Sarma *et al.* [17] and Takahashi *et al.* [36]. The low pCO $_2$ structure was found to be associated with the Transition Zone Chlorophyll Front (TZCF) along the 18°C isotherm in the central North Pacific Ocean [17], [58]. Similarly, a low pCO $_2$ structure (Figs. 7–10) shifts according to the seasonal change of TZCF between 30°N and

45°N [58]. In the polar band, it is seen that in the North Pacific Ocean, a weak pCO $_2$ feature (<340 μ atm) is observed during summer (Fig. 9), a moderate pCO $_2$ feature (340–370 μ atm) during autumn (Fig. 10), and a strong pCO $_2$ feature (370–400 μ atm) during winter and spring (Figs. 7 and 8). Similar pCO $_2$ seasonal trends were observed in the *in-situ* observation data [36] and satellite-derived monthly pCO $_2$ climatological maps [17]. The seasonal variations of surface ocean pCO $_2$ in polar regions are strongly influenced by seasonal variations of biological production (Chl a) rather than SST and SSS [17], [36]. In the North Atlantic Ocean, the pCO $_2$ levels changed with the seasons; for instance, high pCO $_2$ (370–400 μ atm) during winter (Fig. 7) and low pCO $_2$ (<350 μ atm) during spring, summer, and autumn (Figs. 8–10), which are consistent with the observed trends in the pCO $_2$ climatological maps [36]. In contrast, the pCO $_2$ levels are noticeably very low (<330 μ atm) off the west coast of South Atlantic Ocean (near to Brazil) due to the mixing of warm (Brazilian current) and cold (western boundary currents) ocean currents and high biological production in the region. In the tropical and mid-latitude band (45°N–45°S), stratified open ocean waters of South Atlantic Ocean have much higher pCO $_2$ levels (390–430 μ atm) in winter and spring (Figs. 7 and 8) than in summer and autumn (Figs. 9 and 10), which are governed by the effects of stratification, thermodynamic, horizontal, and vertical gradients of SST and SSS [8], [12], [17], [36]. Such large areas of high pCO $_2$ fields in winter and spring and small areas of low pCO $_2$ fields in winter and spring were earlier reproduced in the monthly pCO $_2$ climatological maps [36].

Similarly, higher pCO $_2$ levels occupied small areas of the North Atlantic Ocean (390–430 μ atm) in winter and spring (Figs. 7 and 8) and large areas (390–430 μ atm) in summer and autumn (Figs. 9 and 10), which are consistent with the monthly pCO $_2$ climatological maps [36], despite the computed pCO $_2$ values in the present study being approximately 10–30 μ atm higher than their pCO $_2$ values. These seasonal variations of surface ocean pCO $_2$ in tropical and subtropical regions of both the hemispheres are strongly influenced by SST and SSS rather than the biological effects [8], [12], [17], [36]. High pCO $_2$ fields are observed in the Pacific Ocean (370–430 μ atm) and seasonally stratified regions (390–430 μ atm) in both the hemispheres (Figs. 7–10) where seasonal salinity structures are observed in the Aquarius SSS products. The stratified high pCO $_2$ structures are invisible in the climatological maps of Takahashi *et al.* [36]. The Southern Indian Ocean has very high pCO $_2$ patches (>410 μ atm) in all the seasons due to the strong upwelling/vertical mixing which was not observed in Takahashi *et al.* [36] monthly pCO $_2$ climatological pCO $_2$ maps.

In contrast, the Bay of Bengal (BOB) is one of the largest marginal seas of the Indian Ocean strongly influenced by the southwest and northeastern monsoon systems. During the southwest monsoon (June–August), this region experiences high precipitation and river inputs, leading to low surface salinities and strong stratification [59]. Despite the river inputs affecting most coastal areas, the open-sea regions of BOB are generally devoid of nutrients and hence low biological productivity (low Chl a) [60], [61]. As a result, the pCO $_2$ in BOB waters is increased during January–March (northeastern monsoon) (>420 μ atm) due to the lower biological productivity, vertical

mixing, and high inflow of organic and inorganic carbon through the river systems.

V. CONCLUSION

A multiparametric nonlinear regression (MPNR) is presented here for the estimation of global-scale distribution of surface ocean pCO₂ using satellite-derived SST, SSS, and Chl_a. Unlike the earlier models developed using limited *in-situ* data and multiple/discrete regression equations for limited locations and few confirmed pCO₂ trends, this study has demonstrated the robustness of the MPNR in providing continuous coverage of pCO₂ with a greater accuracy using satellite-derived physical (SST, SSS) and biological (Chl_a) data. The measured *in-situ* pCO₂ fields over the basin- and global-scales showed large variability in the equatorial and tropical domains, and subtropical and polar oceans despite their strong seasonal amplitudes and east–west gradients due to physical and biological conditions. Our analysis showed that spatial and seasonal changes in the global surface ocean pCO₂ fields are closely in phase with the SST structures as previously confirmed by other studies [12], [62]–[64]. It was observed that the temperate, subpolar, and polar regions exhibit large seasonal SST changes due to the solar radiation input, ocean circulation and vertical mixing, and heat exchange between the ocean–atmosphere system. Consequently, the difference in pCO₂ amplitudes may be solely attributed to SST changes on long time scales, but the effect of ocean circulation and biological activity causes persistent CO₂ sinks in certain regional oceanic regimes. The pCO₂ trends in such complex oceanic regimes are difficult to discern from the regional models and require a multiparametric approach that accounts for all the controlling factors to accurately estimate pCO₂ in global oceans. The MPNR approach developed here is a promising tool for the estimation of pCO₂ fields on basin- and global scales using satellite-derived SST, SSS, and Chl_a data, as these products are readily available in the most oceanic regions and represent the dominant processes of thermodynamics, physical mixing, and biological production.

The pCO₂ fields displayed strong positive and negative relations with the physical and biological parameters in the polar and subpolar bands, where pCO₂ changes are inversely correlated with Chl_a caused by the photosynthetic drawdown and positively correlated with Chl_a caused by vertical mixing, upwelling, and respiration within the mixed layer. The influence of solubility (thermodynamic) and dilution by fresh water has been observed to have a positive relation of pCO₂ with SST in the tropical and subtropical bands. In the polar and subpolar bands, pCO₂ changes are inversely correlated with SST due to the increased solubility of CO₂ in cold waters (low SST) than in warm waters (high SST). These changes are well captured by changes in SST, SSS, and Chl_a over the different oceanic regimes using the MPNR approach presented in this study. *In-situ* validation data showed that the MPNR reproduced observed pCO₂ levels within an RMSE of 5.35–8.48 μatm and R² values of 0.86–0.93. Further application to satellite-derived SST, SSS, and Chl_a showed that variations in pCO₂ along several cruise transects were well reproduced by satellite pCO₂ within an RMSE of 6.12–8.77 μatm and R² values of 0.82–0.91. Compared with

earlier studies, the monthly and seasonal amplitudes of pCO₂ changes observed in the satellite-derived products are closely consistent with the climatological distribution of pCO₂ for the corresponding year 2014 and locations in addition to providing new insights in regional differences in the influences of physical and biological processes.

It should be mentioned that the biological activity plays a vital role in controlling pCO₂ variations in polar, subpolar and equatorial, and upwelling dominated regions. However, no *in-situ* Chl_a data are contained in the datasets provided by NODC-NOAA to examine the regional differences. Considering the scarcity of *in-situ* measured Chl_a data, we used MODIS-Aqua data to generate matchup data corresponding to the pCO₂ measurements along the cruise transects in the Atlantic, Pacific, and Southern Oceans. The satellite-derived pCO₂ using MPNR generally better agreed with *in-situ* pCO₂ observations in different ocean basins within an error of less than 7.56 μatm. However, the MPNR approach is robust globally, but it is probably not as accurate as the regional models that are published in the previous pCO₂ studies. Further improvement of the MPNR can be made by using concurrent measurements of pCO₂, SST, SSS, and Chl_a in global oceanic waters. In this process, it may be necessary to incorporate additional parameters such as MLD, CDOM, PAR, NPP, phytoplankton functional types (PFT), wind speed and direction, and specific pCO₂ changes associated with special events across small spatial scales (i.e., eddy effects, phytoplankton blooms, and typhoons). MLD plays an essential role in understanding the effect of episodic events, such as hurricanes, storms, frontal, and eddy driven upwelling processes that can alter the pCO₂ variations at the sea surface by pumping the subsurface waters into the surface mixed layer of the ocean [65], and also mixed layer dynamics of the upper ocean which is forced with wind and heat fluxes. Similarly, CDOM is one of the major contributors to the absorption budget of most freshwater systems and can be used as a proxy to assess nonoptical carbon fractions, such as dissolved organic carbon (DOC) and pCO₂ [66]. Freshwater systems also contain a large amount of carbon dioxide (CO₂) relative to the atmosphere [67], and the ability to assess both DOC and pCO₂ from the CDOM optical properties opens further perspectives on the use of ocean color remote sensing data for monitoring carbon dynamics in large running water systems worldwide [66]. CDOM, more likely adapted to the development of ocean color remote sensing-based pCO₂ inversion algorithms, has been also considered as a potential proxy of pCO₂ [25], [68], [69]. CDOM can be used as either direct driver [66], [70] or proxy for salinity/riverine inputs, which are used to estimate pCO₂ [25]. In the future, spatial and temporal accuracies of surface ocean pCO₂ estimations would be further improved by incorporating the other related parameters governing the pCO₂ distributions.

ACKNOWLEDGMENT

The authors were very thankful to the *in-situ* pCO₂ data contributors (U. Schuster, A.J. Watson, V. Kitidis, S. Nakaoka, K. Sullivan, R. Wanninkhof, A. Murata, J. Akl, C. Neill, B. Tilbrook, N. Metzl, C.E. Cosca, S.R. Alin, R.A. Feely, and S. van Heuven), who have collected, processed, quality controlled, and contributed to the NODC-NOAA database. They would also

like to acknowledge the Ocean Biology Processing Group of GSFC-NASA for the support of the SeaDAS software and distribution of the MODIS-Aqua and Aquarius and the JPL-NASA for the distribution of the SMAP data. They were also grateful to Dr. Taro Takahashi for the contribution of climatological maps of surface ocean pCO₂ that captured basin-scale and global geographical structures of surface ocean pCO₂. They also sincerely would like to thank the anonymous reviewers for their constructive comments and suggestions.

REFERENCES

- [1] B. Ekwurzel *et al.*, "The rise in global atmospheric CO₂, surface temperature, and sea level from emissions traced to major carbon producers," *Clim. Change*, vol. 144, no. 4, pp. 579–590, 2017.
- [2] A. R. Fay and G. A. McKinley, "Global trends in surface ocean pCO₂ from in situ data," *Global Biogeochem. Cycles*, vol. 27, no. 2, pp. 541–557, 2013.
- [3] T. Tyrrell, "Anthropogenic modification of the oceans," *Philos. Trans. R. Soc. A-Math. Phys. Eng. Sci.*, vol. 369, no. 1938, pp. 887–908, 2011.
- [4] T. Crueger, E. Roegner, R. Raddatz, R. Schnur, and P. Wetzel, "Ocean dynamics determine the response of oceanic CO₂ uptake to climate change," *Clim. Dyn.*, vol. 31, no. 2–3, pp. 151–168, 2008.
- [5] A. Schmittner, A. Oschlies, H. D. Matthews, and E. D. Galbraith, "Future changes in climate, ocean circulation, ecosystems, and biogeochemical cycling simulated for a business-as-usual CO₂ emission scenario until year 4000 AD," *Global Biogeochem. Cycles*, vol. 22, no. 1, pp. 1–21, 2008.
- [6] F. Dong, Y. Li, B. Wang, W. Huang, Y. Shi, and W. Dong, "Global air-sea CO₂ flux in 22 CMIP5 models: Multiyear mean and interannual variability," *J. Clim.*, vol. 29, no. 7, pp. 2407–2431, 2016.
- [7] C. Rödenbeck *et al.*, "Global surface-ocean pCO₂ and sea-Air CO₂ flux variability from an observation-driven ocean mixed-layer scheme," *Ocean Sci.*, vol. 9, no. 2, pp. 193–216, 2013.
- [8] T. Takahashi *et al.*, "Climatological mean and decadal change in surface ocean pCO₂, and net sea-air CO₂ flux over the global oceans," *Deep. Res. Part II Top. Stud. Oceanogr.*, vol. 56, no. 8–10, pp. 554–577, 2009.
- [9] R. C. Hamme, D. P. Nicholson, W. J. Jenkins, and S. R. Emerson, "Using noble gases to assess the ocean's carbon pumps," *Ann. Rev. Mar. Sci.*, vol. 11, no. 1, pp. 75–103, 2019, doi: [10.1146/annurev-marine-121916-063604](https://doi.org/10.1146/annurev-marine-121916-063604).
- [10] A. Murata and T. Takizawa, "Summertime CO₂ sinks in shelf and slope waters of the western Arctic Ocean," *Cont. Shelf Res.*, vol. 23, no. 8, pp. 753–776, May 2003, doi: [10.1016/S0278-4343\(03\)00046-3](https://doi.org/10.1016/S0278-4343(03)00046-3).
- [11] T. Volk and M. I. Hoffert, "Ocean carbon pumps: Analysis of relative strengths and efficiencies in ocean-driven atmospheric CO₂ changes," *Carbon Cycle Atmos. CO₂ Nat. Var. Archean Present*, vol. 32, pp. 99–110, 1985.
- [12] T. Takahashi *et al.*, "Global sea-air CO₂ flux based on climatological surface ocean pCO₂, and seasonal biological and temperature effects," *Deep. Res. Part II Top. Stud. Oceanogr.*, vol. 49, pp. 1601–1622, 2002.
- [13] Y. Bai *et al.*, "A mechanistic semi-analytical method for remotely sensing sea surface pCO₂ in river-dominated coastal oceans: A case study from the East China Sea," *J. Geophys. Res. Ocean.*, vol. 120, no. 3, pp. 2331–2349, 2015.
- [14] C. Jamet, C. Moulin, and N. Lef, "Estimation of the oceanic pCO₂ in the North Atlantic from VOS lines *in-situ* measurements: Parameters needed to generate seasonally mean maps," *Ann. Geophys.*, vol. 25, no. 11, pp. 2247–2257, Nov. 2007, doi: [10.5194/angeo-25-2247-2007](https://doi.org/10.5194/angeo-25-2247-2007).
- [15] P. Marrec *et al.*, "Dynamics of air-sea CO₂ fluxes in the North-West European shelf based on voluntary observing ship (VOS) and satellite observations," *Biogeosciences Discuss.*, vol. 12, no. 7, pp. 5641–5695, 2015.
- [16] Y. Rangama *et al.*, "Variability of the net air-sea CO₂ flux inferred from shipboard and satellite measurements in the Southern Ocean south of Tasmania and New Zealand," *J. Geophys. Res. C Ocean.*, vol. 110, no. 9, pp. 1–17, 2005.
- [17] V. V. S. S. Sarma *et al.*, "Basin-scale pCO₂ distribution using satellite sea surface temperature, Chla, and climatological salinity in the North Pacific in spring and summer," *Global Biogeochem. Cycles*, vol. 20, no. 3, pp. 1–13, Sep. 2006, doi: [10.1029/2005GB002594](https://doi.org/10.1029/2005GB002594).
- [18] M. P. Stephens, G. Samuels, D. B. Olson, R. A. Fine, and T. Takahashi, "Sea-air flux of CO₂ in the North Pacific using shipboard and satellite data," *J. Geophys. Res.*, vol. 100, no. C7, 1995, Art. no. 13571.
- [19] T. Ono, T. Saino, N. Kurita, and K. Sasaki, "Basin-scale extrapolation of shipboard pCO₂ data by using satellite SST and Chla," *Int. J. Remote Sens.*, vol. 25, no. 19, pp. 3803–3815, 2004, doi: [10.1080/01431160310001657515](https://doi.org/10.1080/01431160310001657515).
- [20] M. Telszewski *et al.*, "Estimating the monthly pCO₂ distribution in the north Atlantic using a self-organizing neural network," *Biogeosciences*, vol. 6, no. 8, pp. 1405–1421, 2009, doi: [10.5194/bg-6-1405-2009](https://doi.org/10.5194/bg-6-1405-2009).
- [21] M. Chierici, A. Olsen, T. Johannessen, J. Trinañes, and R. Wanninkhof, "Algorithms to estimate the carbon dioxide uptake in the northern North Atlantic using shipboard observations, satellite and ocean analysis data," *Deep. Res. Part II Top. Stud. Oceanogr.*, vol. 56, no. 8–10, pp. 630–639, 2009.
- [22] Y. Zhu, S. Shang, W. Zhai, and M. Dai, "Satellite-derived surface water pCO₂ and air-sea CO₂ fluxes in the northern South China Sea in summer," *Prog. Nat. Sci.*, vol. 19, no. 6, pp. 775–779, 2009.
- [23] L. Gregor, S. Kok, and P. Monteiro, "Empirical methods for the estimation of Southern Ocean CO₂: Support vector and random forest regression," *Biogeosciences*, vol. 14, no. 23, pp. 5551–5569, 2017.
- [24] S. Chen, C. Hu, R. H. Byrne, L. L. Robbins, and B. Yang, "Remote estimation of surface pCO₂ on the West Florida Shelf," *Cont. Shelf Res.*, vol. 128, no. 1, pp. 10–25, Jul. 2016, doi: [10.1016/j.csr.2016.09.004](https://doi.org/10.1016/j.csr.2016.09.004).
- [25] S. E. Lohrenz and W. J. Cai, "Satellite ocean color assessment of air-sea fluxes of CO₂ in a river-dominated coastal margin," *Geophys. Res. Lett.*, vol. 33, no. 1, pp. 2–5, 2006, doi: [10.1029/2005GL023942](https://doi.org/10.1029/2005GL023942).
- [26] S. Nakaoka *et al.*, "Estimating temporal and spatial variation of ocean surface pCO₂ in the North Pacific using a self-organizing map neural network technique," *Biogeosciences*, vol. 10, no. 9, pp. 6093–6106, 2013, doi: [10.5194/bg-10-6093-2013](https://doi.org/10.5194/bg-10-6093-2013).
- [27] G. Parard, A. A. Charantonis, and A. Rutgerson, "Remote sensing the sea surface CO₂ of the Baltic Sea using the SOMLO methodology," *Biogeosciences*, vol. 12, no. 11, pp. 3369–3384, 2015.
- [28] T. Friedrich and A. Oschlies, "Neural network-based estimates of North Atlantic surface pCO₂ from satellite data: A methodological study," *J. Geophys. Res. Ocean.*, vol. 114, no. 3, pp. 1–12, 2009.
- [29] H. Moussa, M. A. Benallal, C. Goyet, and N. Lefèvre, "Satellite-derived CO₂ fugacity in surface seawater of the tropical Atlantic Ocean using a feedforward neural network," *Int. J. Remote Sens.*, vol. 37, no. 3, pp. 580–598, 2016.
- [30] J. Zeng, Y. Nojiri, P. Landschützer, M. Telszewski, and S. Nakaoka, "A global surface ocean fCO₂ climatology based on a feed-forward neural network," *J. Atmos. Ocean. Technol.*, vol. 31, no. 8, pp. 1838–1849, 2014.
- [31] Y. H. Jo, M. Dai, W. Zhai, X. H. Yan, and S. Shang, "On the variations of sea surface pCO₂ in the northern South China Sea: A remote sensing based neural network approach," *J. Geophys. Res. Ocean.*, vol. 117, no. 8, pp. 1–13, 2012.
- [32] S. Chen *et al.*, "A machine learning approach to estimate surface ocean pCO₂ from satellite measurements," *Remote Sens. Environ.*, vol. 228, pp. 203–226, Apr. 2019.
- [33] X. Song *et al.*, "Remote sensing of sea surface pCO₂ in the Bering sea in summer based on a mechanistic semi-analytical algorithm (MeSAA)," *Remote Sens.*, vol. 8, no. 7, pp. 1–25, 2016.
- [34] B. Hales *et al.*, "Satellite-based prediction of pCO₂ in coastal waters of the eastern North Pacific," *Prog. Oceanogr.*, vol. 103, pp. 1–15, 2012.
- [35] B. Hales *et al.*, "Satellite-based prediction of pCO₂ in coastal waters of the eastern North Pacific," *Prog. Oceanogr.*, vol. 103, pp. 1–15, 2012.
- [36] T. Takahashi *et al.*, "Climatological Distributions of pH, pCO₂, Total CO₂, Alkalinity, and CaCO₃ saturation in the global surface ocean, and temporal changes at selected locations," *Mar. Chem.*, vol. 164, pp. 95–125, Aug. 2014, doi: [10.1016/j.marchem.2014.06.004](https://doi.org/10.1016/j.marchem.2014.06.004).
- [37] Z. Li, "Global autocorrelation scales of the partial pressure of oceanic CO₂," *J. Geophys. Res. Ocean.*, vol. 110, no. C8-C08002, pp. 1–12, 2005, doi: [10.1029/2004JC002723](https://doi.org/10.1029/2004JC002723).
- [38] W. T. Liu and X. Xie, "Space observation of carbon dioxide partial pressure at ocean surface," *IEEE J. Sel. Topics Appl. Earth Obs. Remote Sens.*, vol. 10, no. 12, pp. 5472–5484, Dec. 2017.
- [39] H. C. Bittig *et al.*, "An alternative to static climatologies: Robust estimation of open ocean CO₂ variables and nutrient concentrations from T, S, and O₂ data using Bayesian neural networks," *Front. Mar. Sci.*, vol. 5, pp. 1–29, Sep. 2018, doi: [10.3389/fmars.2018.00328](https://doi.org/10.3389/fmars.2018.00328).
- [40] T. Takahashi, S. C. Sutherland, and A. Kozyr, "Global ocean surface water partial pressure of CO₂ database: Measurements performed during 1957–2011 (Version 2011)," Carbon Dioxide Inf. Anal. Center, Oak Ridge Natl. Lab. US Dep. Energy, Oak Ridge, TN, USA, ORNL/CDIAC-160, NDP-088 (V2011), 2012.

- [41] N. R. Bates and J. T. Mathis, "The Arctic Ocean marine carbon cycle: Evaluation of air-sea CO₂ exchanges, ocean acidification impacts and potential feedbacks," *Biogeosciences Discuss.*, vol. 6, no. 4, pp. 6695–6747, 2009, doi: [10.5194/bgd-6-6695-2009](https://doi.org/10.5194/bgd-6-6695-2009).
- [42] V. V. S. S. Sarma, "Monthly variability in surface pCO₂ and net air-sea CO₂ flux in the Arabian Sea," *J. Geophys. Res.*, vol. 108, no. C8, p. 3255, 2003.
- [43] R. A. Fine, D. A. Willey, and F. J. Millero, "Global variability and changes in ocean total alkalinity from Aquarius satellite data," *Geophys. Res. Lett.*, vol. 44, no. 1, pp. 261–267, 2017.
- [44] C. Goyet *et al.*, "Spatial variation of total CO₂ and total alkalinity in the northern Indian Ocean: A novel approach for the quantification of anthropogenic CO₂ in seawater," *J. Mar. Res.*, vol. 57, no. 1, pp. 135–163, 1999.
- [45] A. G. Dickson and C. Goyet, "Handbook of methods for the analysis of the various parameters of the carbon dioxide system in sea water. Version 2," Oak Ridge National Lab., Oak Ridge, TN, USA, Tech. Rep., Sep. 1994, doi: [10.2172/10107773](https://doi.org/10.2172/10107773).
- [46] E. M. Hood, L. Merlivat, and T. Johannessen, "Variations of fCO₂ and air-sea flux of CO₂ in the Greenland Sea gyre using high-frequency time series data from CARIOCA drift buoys," *J. Geophys. Res. Ocean.*, vol. 104, no. C9, pp. 20571–20583, 1999.
- [47] A. D. Berryman, D. Goudiaby, and P. Moore, "A multiple linear regression of pCO₂ against sea-surface temperature, salinity, and chlorophyll a at station ALOHA and its potential for estimate pCO₂ from satellite data," *Elizab. City, NC*, 2008.
- [48] L. Chen *et al.*, "Estimation of monthly air-sea CO₂ flux in the southern atlantic and indian ocean using *in-situ* and remotely sensed data," *Remote Sens. Environ.*, vol. 115, no. 8, pp. 1935–1941, 2011, doi: [10.1016/j.rse.2011.03.016](https://doi.org/10.1016/j.rse.2011.03.016).
- [49] D. A. Siegel *et al.*, "Regional to global assessments of phytoplankton dynamics from the SeaWiFS mission," *Remote Sens. Environ.*, vol. 135, pp. 77–91, 2013.
- [50] K. Drushka, S. T. Gille, and J. Sprintall, "The diurnal salinity cycle in the tropics," *J. Geophys. Res. Ocean.*, vol. 119, no. 9, pp. 5874–5890, 2014.
- [51] E. C. Fine, F. O. Bryan, W. G. Large, and D. A. Bailey, "An initial estimate of the global distribution of diurnal variation in sea surface salinity," *J. Geophys. Res. Ocean.*, vol. 120, no. 5, pp. 3211–3228, 2015.
- [52] X. Wang, R. Murtugudde, E. Hackert, J. Wang, and J. Beauchamp, "Seasonal to decadal variations of sea surface pCO₂ and sea-air CO₂ flux in the equatorial oceans over 1984–2013: A basin-scale comparison of the Pacific and Atlantic Oceans," *Global Biogeochem. Cycles*, vol. 29, no. 5, pp. 597–609, 2015.
- [53] N. Lefèvre and G. F. Moore, "Distribution of the CO₂ partial pressure along an Atlantic meridional transect," *Prog. Oceanogr.*, vol. 45, no. 3–4, pp. 401–413, 2000.
- [54] N. Lefèvre, "Observations of pCO₂ in the coastal upwelling off Chile: Spatial and temporal extrapolation using satellite data," *J. Geophys. Res.*, vol. 107, no. C6, p. 3055, 2002.
- [55] A. Olsen, A. M. Omar, A. C. Stuart-Menteth, and J. A. Triñanes, "Diurnal variations of surface ocean pCO₂ and sea-air CO₂ flux evaluated using remotely sensed data," *Geophys. Res. Lett.*, vol. 31, no. 20, pp. 2–5, 2004.
- [56] K. Wyrtyk, "Oceanography of the Eastern Equatorial Pacific Ocean," *Oceanogr. Marine Biol. Ann. Rev.*, vol. 4, pp. 33–68, 1966.
- [57] P. C. Fiedler, V. Philbrick, and F. P. Chavez, "Oceanic upwelling and productivity in the eastern tropical Pacific," *Limnol. Oceanogr.*, vol. 36, no. 8, pp. 1834–1850, 1991.
- [58] J. J. Polovina, E. Howell, D. R. Kobayashi, and M. P. Seki, "The transition zone chlorophyll front, a dynamic global feature defining migration and forage habitat for marine resources," *Prog. Oceanogr.*, vol. 49, no. 1–4, pp. 469–483, 2001, doi: [10.1016/S0079-6611\(01\)00036-2](https://doi.org/10.1016/S0079-6611(01)00036-2).
- [59] V. N. Murty, A. Suryanarayana, and M. J. Varkey, *Physical Oceanography of the Bay of Bengal*. 1996.
- [60] M. Madhupratap *et al.*, "Biogeochemistry of the Bay of Bengal: Physical, chemical and primary productivity characteristics of the central and western Bay of Bengal during summer monsoon 2001," *Deep. Res. Part II Top. Stud. Oceanogr.*, vol. 50, no. 5, pp. 881–896, 2003.
- [61] M. Tholkapiyan, P. Shanmugam, and T. Suresh, "Monitoring of ocean surface algal blooms in coastal and oceanic waters around India," *Environ. Monit. Assess.*, vol. 186, no. 7, pp. 4129–4137, 2014.
- [62] W. T. Liu and X. Xie, "Ocean surface carbon dioxide fugacity observed from space," in *Proc. 20th Conf. Satellite Meteor. Oceanogr.*, 2014, pp. 1–24.
- [63] C. Sweeney *et al.*, "Spatial and temporal variability of surface water pCO₂ and sampling strategies," *A Large-Scale CO₂ Obs. Plan Situ Ocean. Atmos.*, Tech. Rep., pp. 155–175, 2002.
- [64] P. Xiu and F. Chai, "Variability of oceanic carbon cycle in the North Pacific from seasonal to decadal scales," *J. Geophys. Res. Ocean.*, vol. 119, no. 8, pp. 5270–5288, 2014.
- [65] A. Mahadevan, A. Tagliabue, L. Bopp, A. Lenton, L. Mémerly, and M. Lévy, "Impact of episodic vertical fluxes on sea surface pCO₂," *Philos. Trans. R. Soc. A Math. Phys. Eng. Sci.*, vol. 369, no. 1943, pp. 2009–2025, 2011.
- [66] A. de Matos Valerio *et al.*, "Using CDOM optical properties for estimating DOC concentrations and pCO₂ in the lower Amazon River," *Opt. Express*, vol. 26, no. 14, pp. A657–A677, 2018.
- [67] N. D. Ward *et al.*, "Where carbon goes when water flows: Carbon cycling across the aquatic continuum," *Front. Mar. Sci.*, vol. 4, pp. 1–27, Jan. 2017, doi: [10.3389/fmars.2017.00007](https://doi.org/10.3389/fmars.2017.00007).
- [68] T. Kutser, C. Verpoorter, B. Paavel, and L. J. Tranvik, "Estimating lake carbon fractions from remote sensing data," *Remote Sens. Environ.*, vol. 157, pp. 138–146, 2015.
- [69] C. D. Clark *et al.*, "CDOM distribution and CO₂ production on the Southwest Florida Shelf," *Mar. Chem.*, vol. 89, no. 1–4, pp. 145–167, 2004.
- [70] B. G. T. Else, J. J. Yackel, and T. N. Papakyriakou, "Application of satellite remote sensing techniques for estimating air-sea CO₂ fluxes in Hudson Bay, Canada during the ice-free season," *Remote Sens. Environ.*, vol. 112, no. 9, pp. 3550–3562, 2008.



Kande Vamsi Krishna received B.Tech. degree in Electronics and Communication Engineering (ECE) from the Rajiv Gandhi University of Knowledge Technologies (RGUKT), IIIT Nuzvid, Andhra Pradesh, India, in 2015, and M.Tech. degree in remote sensing from Jawaharlal Nehru Technological University (JNTU), Kakinada, Andhra Pradesh, India, in 2017.

He is currently working as a Ph.D. Scholar with the Department of Ocean Engineering, IIT Madras, Chennai, India. His current research interests include satellite oceanography and the development of algorithms for retrieving useful information from satellite observations.



Palanisamy Shanmugam received the Ph.D. degree in optical remote sensing from Anna University, Chennai, India, in 2002.

He is currently a Professor with the Department of Ocean Engineering, IIT Madras, Chennai, India, where he is involved in the experimental and theoretical studies of the optical properties of natural waters, air-sea interface, and subsea optical processes. He has been a Principle Investigator of several projects funded by the Government of India. His current research interests include developing models for ocean optical studies and retrieval algorithms for multispectral and hyperspectral remote sensing sensors with an emphasis on applications to sediment dynamics, algal blooms, climate change, and marine environmental and coastal processes.



Pullaiahgari Venkata Nagamani received the Ph.D. degree in geophysics from Osmania University, India, in 2016.

She is currently working as a Scientist with Biological Oceanography, Earth and Climate Science Area, NRSC (ISRO), Hyderabad, India, where she is involved in the experimental and theoretical studies of the optical properties of natural waters, air-sea interactions, and coastal carbon dynamics. She is Head, BOD, and Principal Investigator of several projects funded by the Government of India. Her current research interests include developing methodologies for better atmospheric correction for the upcoming ocean colour missions of ISRO by ingesting the NRT meteorological and atmospheric parameters, the development of bio-optical and retrieval algorithms for multispectral and hyperspectral remote sensing sensors for better quantification of chlorophyll in the turbid coastal waters, and the identification of phytoplankton blooms and climate change.